nature aging

Resource

https://doi.org/10.1038/s43587-024-00799-6

Sex-specific and cell-type-specific changes in chaperone-mediated autophagy across tissues during aging

Received: 18 May 2024

Accepted: 18 December 2024

Published online: 05 February 2025

Check for updates

Rabia R. Khawaja[1,2,10] ✉, Adrián Martín-Segura[1,2,7,10], Olaya Santiago-Fernández[1,2], Rebecca Sereda[1,2], Kristen Lindenau[1,2], Mericka McCabe[1,2,3], Adrián Macho-González[1,2], Maryam Jafari[1,2], Aurora Scrivo[1,2,8], Raquel Gomez-Sintes[1,2,9], Bhakti Chavda[1,2], Ana Rosa Saez-Ibanez[1,2], Inmaculada Tasset[1,2,4], Esperanza Arias[2,5], Xianhong Xie[6], Mimi Kim[6], Susmita Kaushik[1,2] & Ana Maria Cuervo[1,2,5] ✉

Aging leads to progressive decline in organ and tissue integrity and function, partly due to loss of proteostasis and autophagy malfunctioning. A decrease with age in chaperone-mediated autophagy (CMA), a selective type of lysosomal degradation, has been reported in various organs and cells from rodents and humans. Disruption of CMA recapitulates features of aging, whereas activating CMA in mice protects against age-related diseases such as Alzheimer's, retinal degeneration and/or atherosclerosis. However, sex-specific and cell-type-specific differences in CMA with aging remain unexplored. Here, using CMA reporter mice and single-cell transcriptomic data, we report that most organs and cell types show CMA decline with age, with males exhibiting a greater decline with aging. Reduced CMA is often associated with fewer lysosomes competent for CMA. Transcriptional downregulation of CMA genes may further contribute to CMA decline, especially in males. These findings suggest that CMA differences may influence organ vulnerability to age-related degeneration.

The functional decline of organs and tissues with age increases the risk of diseases such as neurodegenerative diseases, cardiovascular and metabolic disorders and cancer[1]. Identifying tissue-specific molecular changes with age can enable gerotherapeutic interventions to slow aging and prevent these diseases. Loss of proteostasis with age contributes to tissue dysfunction and degenerative conditions[2]. This work focuses on autophagy, an essential component of the proteostasis network, whose malfunctioning has been associated with the loss of functional integrity in aging tissues[3,4].

Autophagy contributes to cellular homeostasis by degrading dysfunctional cellular components in lysosomes[3,5]. Three types of autophagy co-exist in most mammalian cells. Macroautophagy and microautophagy mediate lysosomal degradation of cargo previously sequestered inside vesicles[5]. Chaperone-mediated autophagy (CMA) ensures selective degradation of proteins by directly translocating them across the lysosomal membrane[6]. CMA substrates contain a KFERQ-like targeting motif used by heat shock cognate protein of 71 kDa (Hsc70) to target them to the lysosome-associated membrane protein type 2A (LAMP2A), the main component of the lysosomal CMA translocation complex[6].

Macroautophagy malfunctions with age, and preventing this decline can extend lifespan and healthspan in various experimental models[7]. Reduced transcription of macroautophagy genes and defective autophagosome–lysosome fusion contribute to its age-related decline in brain and liver[3,8–10]. However, aging may impact macroautophagy in a tissue-specific manner: it increases in white adipose tissue[11]

A full list of affiliations appears at the end of the paper. ✉e-mail: rabia.khawaja@einsteinmed.edu; ana-maria.cuervo@einsteinmed.edu

and kidney proximal tubules and remains unchanged in glomeruli[12–14]. Aging may also affect selective macroautophagy types differently. For example, mitophagy increases with age in the brain, retina, liver and kidney, but it remains unchanged in skeletal myofibers, pancreas and lungs[15]. Endosomal microautophagy (eMI) also declines with age, resulting in reduced degradation and increased extracellular release of undegraded material[16].

Reduced CMA activity with age has been reported in rat and mouse (C57BL/6 and FVB) liver[17,18], hematopoietic stem cells[19], T cells[20] and primary mouse and human fibroblasts in culture[17,18]. Reduced levels of LAMP2A have been identified as the main cause for functional decline of CMA. However, although reduced *Lamp2a* transcription is mostly responsible for the decline of CMA with age in T cells[20], reduced lysosomal stability of LAMP2A, due to changes in lipid composition, is the primary cause of CMA failure in hepatocytes and fibroblasts[18,21]. CMA malfunction also occurs in age-related diseases such as Alzheimer's disease (AD)[22], Parkinson's disease[23,24], diabetes mellitus[25] and atherosclerosis[26]. Organ-specific blockage of CMA in young mice mimics age-related degeneration and dysfunction in the brain[22], liver[27], vasculature[26], T cells[20], adipose tissue[28] and hematopoietic stem cells[19]. Conversely, genetic or pharmacological restoration of CMA protects against retinal degeneration[29], neurodegeneration[22], atherosclerosis[26] and age-related decline in hepatic[30], hematopoietic stem cell[19] and T cell function[20,31].

Given the tissue-specific impact of CMA blockage[20,22,26,27] and the differences in age-related degeneration among tissues, we investigated tissue-specific and cell-specific changes in CMA activity with age that could account for these differences. Although recent studies showed differences in basal CMA activity among liver, adipose tissue and kidney[32], the impact of aging on CMA in most tissues remains unknown. In addition, the use of biochemical procedures in whole organ lysates has precluded studying cell-specific differences in CMA. Furthermore, despite well-established sex differences in mammalian lifespan[33] and the localization of the *Lamp2* gene on the X chromosome, which has been linked to longevity[34], sex differences in basal CMA and in its aging-related changes remain unexplored.

In this work, we investigated cell-type-specific, tissue-specific and sex-specific differences in CMA activity during aging using mice systemically expressing a fluorescent CMA reporter[32]. We found that most cell types exhibited reduced CMA with age, with greater overall decline in males. Combining data from the Tabula Muris Senis single-cell transcriptomic atlas[35] and direct analysis of the endolysosomal compartment, we investigated the transcriptional and post-transcriptional nature of the observed CMA changes. Transcriptional reduction in CMA with age is more pronounced in males. Post-transcriptional decline often resulted from fewer endolysosomal compartments allocated to this pathway and, to a lesser extent, fewer total endolysosomes. Our findings reveal sex-specific differences in baseline CMA activity and in the impact of aging across organs, offering insights for precision medicine interventions in age-related diseases.

Results

Cell-type-specific changes in CMA in the aging brain

We previously generated a transgenic mouse systemically expressing a fluorescent reporter for monitoring CMA activity in vivo[32,36], which was extensively used to analyze CMA in physiological processes such as circadian rhythm[37], stem cell activation[19] or adipogenesis[28] and in pathologies such as neurodegeneration[22], retinal degeneration[29] or atherosclerosis[26]. The reporter protein, constructed by tagging the CMA-targeting motif KFERQ to the fluorescent protein Dendra2 (^{KFERQ}Dendra or ^{K}Dendra), highlights lysosomes as fluorescent puncta when delivered there by CMA[36]. Quantification of the number of fluorescent puncta per cell informs on changes in CMA activity[32,36]. Labeling lysosomes with a general endolysosomal marker such as LAMP1 (L1) allows confirmation that the fluorescent puncta are indeed lysosomes and allows us to determine the fraction of lysosomes engaged in CMA, because only lysosomes bearing Hsc70 in their lumen are competent for CMA[38].

Loss of proteostasis is common in the aging brain[39], and CMA blockage in young mouse neurons leads to collapse of their metastable proteome[22]. However, how aging affects CMA in different brain cell types remains unknown. To identify possible cell-type-specific and region-specific changes in CMA activity with age, we analyzed cortex and hippocampus regions of a cohort of young (4–6 months) and old (24–28 months) male and female ^{KFERQ}Dendra mice (Fig. 1, Extended Data Fig. 1 and Supplementary Fig. 1). We quantified CMA activity as ^{KFERQ}Dendra fluorescent puncta co-localizing with LAMP1 (^{K}Dendra^{+}LAMP1^{+}) and calculated the fraction of lysosomes competent for CMA as the percentage of total LAMP1^{+} puncta positive for the ^{KFERQ}Dendra signal ((^{K}Dendra^{+}LAMP1^{+} / LAMP1^{+}) × 100). Given the higher intercellular heterogeneity in aging, we analyzed data per individual cell to gain information on changes in variance (all reported in Supplementary Table 1). Analyses per animal that take into consideration the correlation in data from cells from the same animal are included in Supplementary Figs. 2–4 and support similar trends as the per-cell analysis shown in the main figures.

Analysis of neuronal CMA activity in the CA1 (Fig. 1a–d) and dentate gyrus (DG; Fig. 1e–h) regions of the hippocampus and in the somatosensory cortex (Fig. 1i–l) and entorhinal cortex (Fig. 1m–p) revealed higher CMA activity in young females than young males in CA1 hippocampus (Fig. 1a,b) (NeuN^{+}CAMKIIα^{+} excitatory neurons and Calbindin^{+} inhibitory neuron markers are shown in Extended Data Fig. 1a–c, and full-field images are shown in Supplementary Fig. 1), which coincides with higher overall number of endolysosomes (L1^{+}) in this region in females (Fig. 1d). Neuronal CMA activity decreased significantly with age in both sexes in the hippocampal regions (Fig. 1b,f) and only in males in the somatosensory cortex (Fig. 1j), whereas it increased in the entorhinal cortex (Fig. 1n). To compare the magnitude of changes in neuronal CMA with age across brain regions, we calculated it as fold of that in young mice and noted a more pronounced decline in CMA in hippocampal neurons in both sexes, with the highest CMA

Fig. 1 | Sex-specific and brain-region-specific changes in neuronal CMA activity with age. a–**p**, CMA activity and endolysosomal changes in CA1 pyramidal neurons (**a**–**d**), DG granule neurons (**e**–**h**), NeuN^{+} neurons in primary somatosensory cortex (S1, **i**–**l**) and NeuN^{+} neurons in entorhinal cortex (EC, **m**–**p**) in young (4–6 m) and old (24–28 m) female and male ^{KFERQ}Dendra mice. Confocal images show neurons stained for ^{K}Dendra and LAMP1 in the indicated regions of hippocampus (**a**,**e**) and cortex (**i**,**m**). Scale bars, 5 µm. Quantification in neurons of the number of ^{K}Dendra^{+}LAMP1^{+} puncta per cell (**b**,**f**,**j**,**n**), the percentage of total LAMP1^{+} puncta also positive for ^{K}Dendra (**c**,**g**,**k**,**o**) and the number of LAMP1^{+} puncta per cell in neurons (**d**,**h**,**l**,**p**). Mean ± s.e.m and individual values are shown. **q**, Quantification of changes in ^{K}Dendra^{+}LAMP1^{+} puncta in neurons in the indicated brain regions of old animals of **a**–**p** figures relative to sex-matched young mice. Values are mean ± s.e.m. **r**,**s**, CMA score from hippocampus (**r**) and cortex neurons (**s**) in young (3 m) and old (18–24 m) female and male mice, calculated from Tabula Muris Senis single-cell RNA-seq data. Boxes: median and 25th and 75th percentiles. Whisker ends: 25th and 75th percentiles ± 1.5 times the IQR. **t**, Colorimetric quantitative graphical representation of average CMA activity (^{K}Dendra^{+}LAMP1^{+} puncta/cell) in neurons of hippocampus and cortex in young and old, female and male mice. Number of mice (cells) for YF, OF, YM and OM, respectively: **b**–**d**, **f**–**h**, **n**–**p**, **q**: 5 (100), 8 (160), 5 (100), 8 (160); **j**–**l**, **q**: 5 (50), 8 (80), 5 (50), 8 (80); **r**: 3 (4), 2 (8), 4(12), 5 (71), **s**: 2 (4), 2 (29), 3 (38), 5 (107). *P* values were calculated using two-way ANOVA with Bonferroni's multiple comparison test. Only significant comparisons are shown. Lower magnification full-field images for **a**, **e**, **i** and **m** are shown in Supplementary Fig. 1a–d, and per-animal values are shown in Supplementary Fig. 2a–d. Number of cells counted per tissue and per animal are in Source Data Fig. 1. m, months; OF, old female; OM, old male; YF, young female; YM, young male.

https://doi.org/10.1038/s43587-024-00799-6

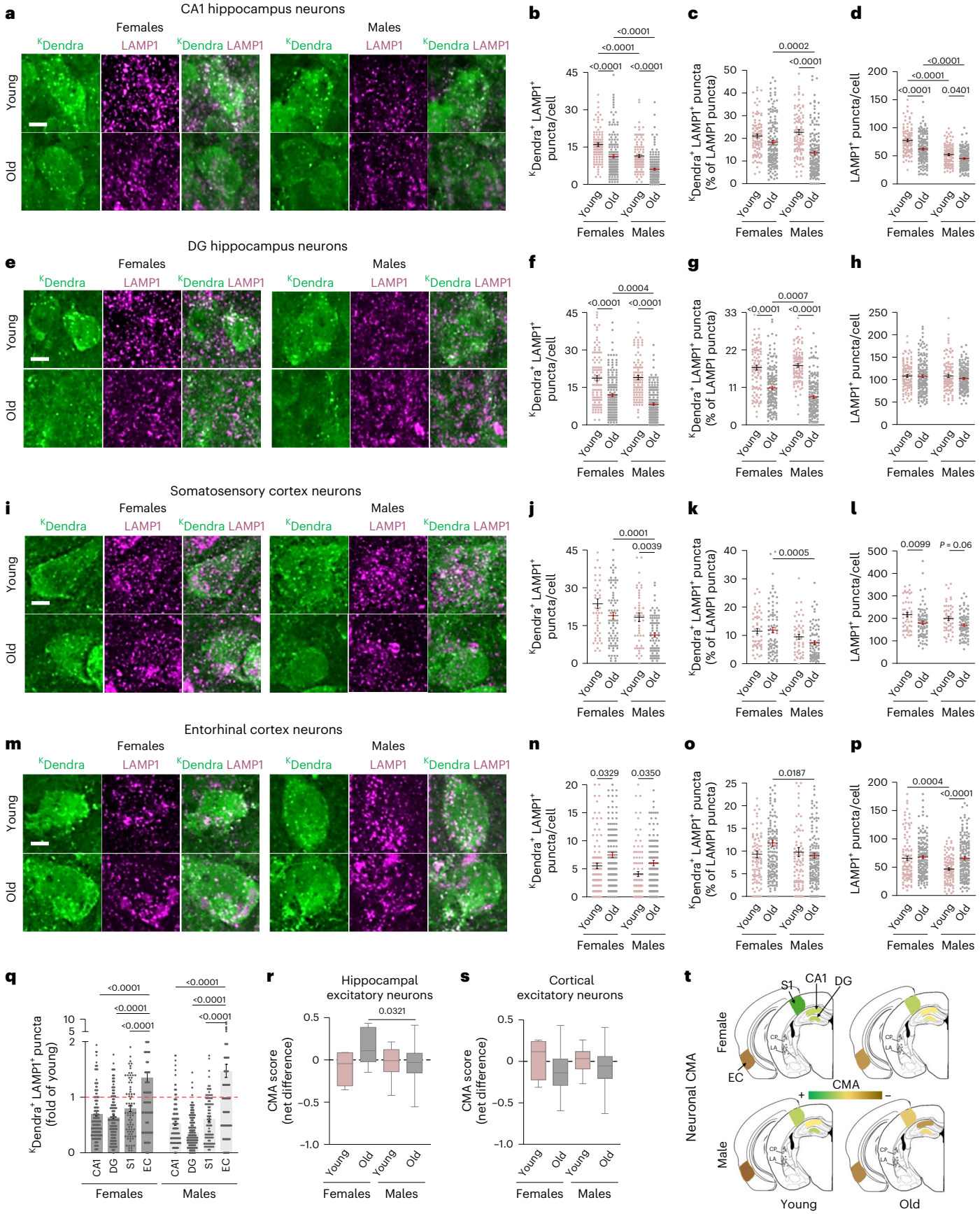

https://doi.org/10.1038/s43587-024-00799-6

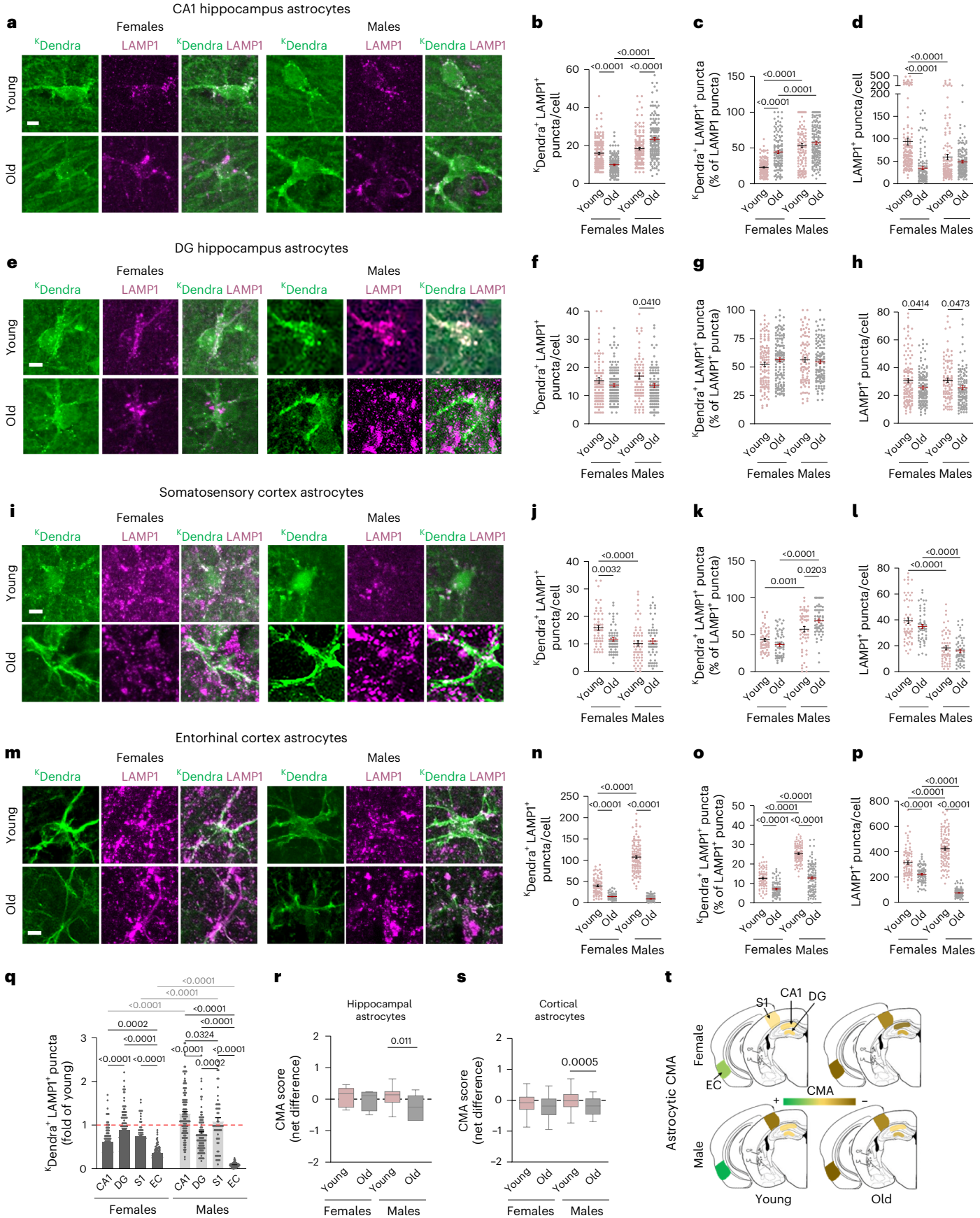

https://doi.org/10.1038/s43587-024-00799-6

Fig. 2 | Sex-specific and brain-region-specific changes in astrocytic CMA activity with age. a–**p**, CMA activity and endolysosomal changes in astrocytes in CA1 (**a**–**d**), DG (**e**–**h**), primary somatosensory cortex (S1, **i**–**l**) and entorhinal cortex (EC, **m**–**p**) in young (4–6 m) and old (24–8 m) female and male ^{KFERQ}Dendra mice. Confocal images show astrocytes stained for ^{K}Dendra and LAMP1 in the indicated regions of hippocampus (**a**,**e**) and cortex (**i**,**m**). Scale bars, 5 µm. Quantification in astrocytes of the number of ^{K}Dendra^{+}LAMP1^{+} puncta per cell (**b**,**f**,**j**,**n**), the percentage of total LAMP1^{+} puncta also positive for ^{K}Dendra (**c**,**g**,**k**,**o**) and the number of LAMP1^{+} puncta per cell (**d**,**h**,**l**,**p**). Mean ± s.e.m. and individual cell values and are shown. **q**, Quantification of changes in ^{K}Dendra^{+}LAMP1^{+} puncta in astrocytes in the indicated brain regions of old animals of **a**–**p** figures relative to sex-matched young mice. Values are mean ± s.e.m. **r**,**s**, CMA score from hippocampus and cortex astrocytes in young (3 m) and old (18–24 m) female and male mice, calculated from Tabula Muris Senis single-cell RNA-seq data. Boxes: median and 25th and 75th percentiles. Whisker ends: 25th and 75th percentiles ± 1.5 times the IQR. **t**, Colorimetric quantitative graphical representation of average CMA activity (^{K}Dendra^{+}LAMP1^{+} puncta/cell) in astrocytes of hippocampus and cortex in young and old, female and male mice. Number of mice (cells) for YF, OF, YM and OM, respectively: **b**–**d**,**q**: 5 (143), 6 (117), 5 (131), 5 (145); **f**–**h**,**q**: 5 (114), 6 (130), 5 (90), 5 (120) cells; **j**–**l**,**q**: 4 (56), 4 (58), 4 (56), 4 (58); **n**–**p**,**q**: 4 (79), 4 (84), 5 (109), 5 (117); **r**: 3 (10), 1 (4), 4 (85), 3 (5); **s**: 1 (52), 2 (64), 3 (221), 3 (38). *P* values were calculated using two-way ANOVA with Bonferroni's multiple comparison test. Only significant comparisons are shown. Lower magnification full-field images for **a**, **e**, **i** and **m** are shown in Supplementary Fig. 1e–h, and per-animal values are shown in Supplementary Fig. 2e–h. Number of cells counted per tissue and per animal are in Source Data Fig. 2. m, months; OF, old female; OM, old male; YF, young female; YM, young male.

reduction observed in male DG neurons (Fig. 1q). As reported for other functional readouts, we observed higher intercellular heterogeneity in CMA activity with age, which was especially noticeable in males (Supplementary Table 1).

Interestingly, the significantly lower overall neuronal CMA activity in old males than in females (Fig. 1b,f,j) could be explained, in part, by consistently fewer neuronal lysosomes dedicated to CMA in the old animals. Thus, we found lower fraction of endolysosomal compartments (L1^{+}) positive for ^{KFERQ}Dendra in aging males compared to females in all brain regions analyzed (Fig. 1c,g,k,o), even when often the total endolysosome number was similar or exhibited lower magnitude changes (Fig. 1d,h,l,p and Extended Data Fig. 1d). Fewer CMA-competent lysosomes could also be behind the reduced neuronal CMA activity in old female DG hippocampus (Fig. 1g).

Because not all cell-type-specific and sex-specific changes in neuronal CMA with age were associated with differences in the fraction of CMA-competent lysosomes, we next investigated possible age-related changes in the CMA transcriptional program. We used the Tabula Muris Senis single-cell transcriptomic atlas of aging mouse tissues[35] and extracted the expression level of all the genes in the CMA network. We used these values to calculate a predictive transcriptional CMA score, as described previously[22], by giving each gene expression value a weight (depending on their relevance on CMA) and directionality (as activator or inhibitor of CMA). We found transcriptional upregulation of CMA components (including *Lamp2* and other key effectors) and overall CMA score in old female hippocampal neurons, not observed in old males (Fig. 1r and Extended Data Fig. 1e). This transcriptional upregulation could explain why old females display a lower decrease in hippocampal CMA than males despite reduced endolysosome number, highlighting that transcriptional changes could be responsible for sex differences in neuronal CMA with age. We did not find transcriptional differences in the CMA network with age or sex in the cortical neurons (Fig. 1s and Extended Data Fig. 1e), although a trend to transcriptional downregulation of CMA-related genes may drive the discrete reduction of CMA activity with age observed in some cortical neurons (Fig. 1j). A colorimetric quantitative representation of sex differences in neuronal CMA activity and changes with age is shown in Fig. 1t to illustrate the overall lower neuronal CMA activity in the male brain and the higher impact of aging in the hippocampal regions.

To determine if changes in CMA activity in the brain were cell type specific, we next analyzed CMA in astrocytes in the same brain regions (Fig. 2). Young brains displayed no differences in astrocytic CMA activity between males and females in hippocampus (Fig. 2a,b,e,f), but, in the cortex, we observed opposite trends with higher CMA activity in females in the somatosensory cortex (Fig. 2i,j) and lower CMA activity in the entorhinal cortex, which displayed the highest astrocytic CMA activity (Fig. 2m,n). Contrary to neurons, where the negative impact of aging was more pronounced in the hippocampal regions, the decline in CMA activity in astrocytes was more evident in both males and females in entorhinal cortex (Fig. 2m,n and comparison of the aging effect in Fig. 2q,t). In the other brain regions, changes with age in astrocytic CMA showed sex-specific differences, with reductions in CMA more noticeable in females, especially around the CA1 region, where, in clear contrast, CMA increased with age in males (Fig. 2b). As in neurons, astrocytes displayed higher intercellular heterogeneity in CMA with age, with more pronounced heterogeneity in the female brains (Supplementary Table 1).

Contrary to the minor changes in endolysosome number with age in neurons, astrocytes displayed sex-dependent marked reduction in number of endolysosomes that, for the most part, correlated with sex-specific and region-specific changes in CMA activity (Fig. 2d,h,l,p and Extended Data Fig. 1d,f). In contrast, the percentage of CMA-active lysosomes only added to the reduction in overall CMA activity in the entorhinal cortex (Fig. 2c,g,k,o), suggesting that lysosome number may be rate limiting for CMA in astrocytes. In fact, we found that neuronal CMA highly correlated with both CMA-competent lysosomes and total endolysosome number, whereas astrocytic CMA mostly correlated with endolysosome number (Extended Data Fig. 1f). As in neurons, we noted a transcriptional downregulation with age of CMA-related genes in both sexes in cortical astrocytes but only in males in the hippocampus

Fig. 3 | Sex-specific and cell-type-specific changes in CMA activity with age in specialized neurons in cerebellum and retina. a–**h** and **m**–**t**, CMA activity and endolysosomal changes in cerebellum inhibitory Purkinje neurons (**a**–**d**) and excitatory granule neurons (**e**–**h**) and in retina photoreceptors, rods (**m**–**p**) and cones (**q**–**t**), from young (4–6 m) and old (24–28 m) female and male ^{KFERQ}Dendra mice. Confocal images show Purkinje (**a**) and granule (**e**) neurons and photoreceptors rods (**m**) and cones (**q**) stained for ^{K}Dendra and LAMP1. Scale bars, 5 µm. Number of ^{K}Dendra^{+}LAMP1^{+} puncta per cell (**b**,**f**,**n**,**r**), percentage of LAMP1^{+} puncta also positive for ^{K}Dendra (**c**,**g**,**o**,**s**) and number of LAMP1^{+} puncta per cell (**d**,**h**,**p**,**t**). Individual cell values and mean ± s.e.m. are shown. **i**, Quantification of changes in ^{K}Dendra^{+}LAMP1^{+} puncta in cerebellum Purkinje and granule neurons from old mice relative to sex-matched young mice. Values are mean ± s.e.m. **j**,**k**, CMA score in inhibitory (Purkinje, **j**) and excitatory (granule, **k**) neurons from cerebellum of young (3 m) and old (18–24 m) female and male mice, calculated from Tabula Muris Senis single-cell RNA-seq data. Boxes: median and 25th and 75th percentiles. Whisker ends: 25th and 75th percentiles ± 1.5 times the IQR. **l**, Colorimetric quantitative graphical representation of average CMA activity (^{K}Dendra^{+}LAMP1^{+} puncta/cell) in cerebellum inhibitory and excitatory neurons in young and old, female and male mice. Number of mice (cells) for YF, OF, YM and OM, respectively: **b**–**d**,**i**: 5 (25), 8 (45), 5 (25), 8 (40); **f**–**i**: 5 (100), 8 (160), 5 (100), 8 (160); **j**: 3 (29), 1 (18), 3 (54), 3 (76); **k**: 3 (11), 2 (34), 4 (81), 4 (54); **n**–**p**: 5 (100), 4 (80), 5 (100), 4 (80); **r**–**t**: 5 (100), 5 (90), 5 (100), 5 (110). *P* values were calculated using two-way ANOVA with Bonferroni's multiple comparison test. Only significant comparisons are shown. Lower magnification full-field images for **a** and **e** are shown in Supplementary Fig. 1i,j and for **m** and **q** in Supplementary Fig. 1k,l. Per-animal values are shown in Supplementary Fig. 2i,j for cerebellum cells and in Supplementary Fig. 2k,l for retinal cells. Number of cells counted per tissue and per animal are in Source Data Fig. 3. m, months; OF, old female; OM, old male; YF, young female; YM, young male.

https://doi.org/10.1038/s43587-024-00799-6

(Fig. 2r,s and Extended Data Fig. 1e). These transcriptional changes may add to the CMA changes driven by endolysosome number.

The cerebellum, one of the brain regions with higher concentration of neurons, has been traditionally overlooked in aging research and considered resistant to AD pathology. However, a recent consensus paper highlighted important functional changes and extensive neuronal loss in cerebellum with age and to the cerebellar accumulation of diffuse forms of beta-amyloid early in AD[40]. To gain insights into changes with

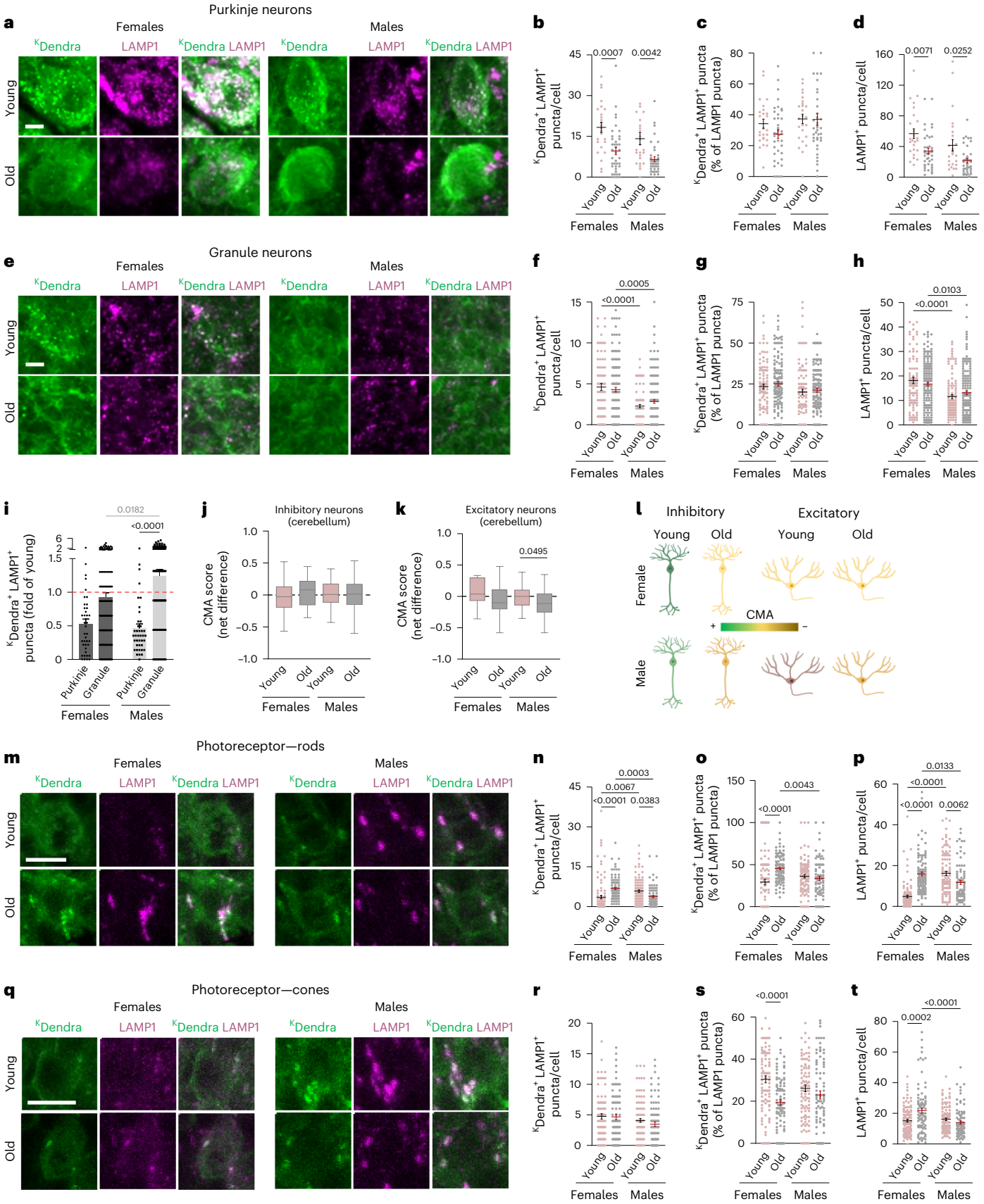

https://doi.org/10.1038/s43587-024-00799-6

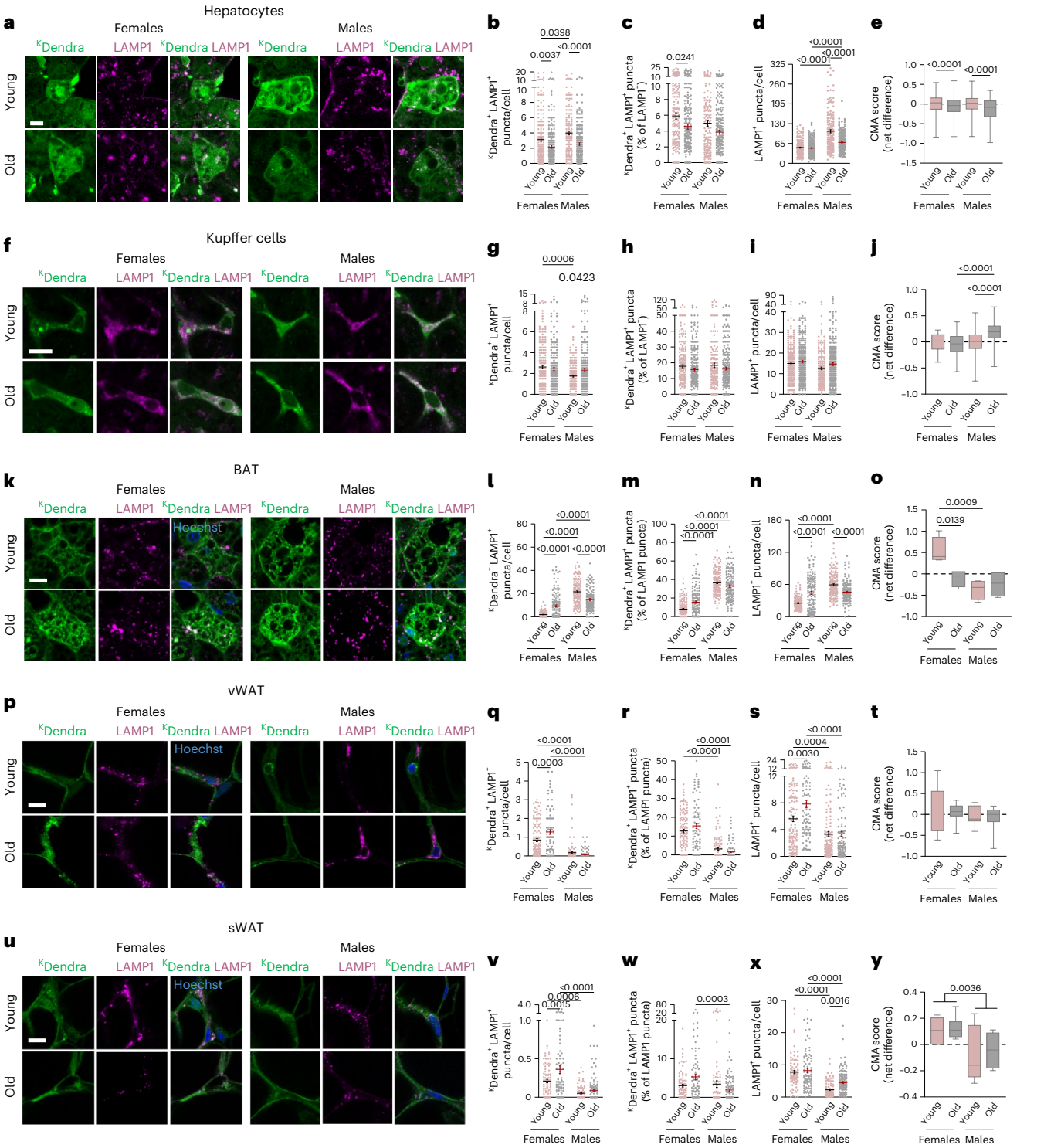

Fig. 4 | Sex-specific and cell-type-specific changes in CMA activity in aging liver and adipose tissues. a–**y**, CMA activity and endolysosomal changes in liver (**a**–**j**), brown adipose tissue (BAT, **k**–**o**) and visceral (v) and subcutaneous (s) white adipose tissue (WAT, **p**–**y**) in young (4–6 m) and old (24–28 m) female and male ^{KFERQ}Dendra mice. Representative confocal images show hepatocytes (**a**), Kupffer cells (**f**) and adipocytes (**k**,**p**,**u**) stained for ^{K}Dendra and LAMP1. Hoechst is also shown to delineate adipocytes (**k**,**p**,**u**). Scale bars, 10 µm. Quantification of ^{K}Dendra^{+}LAMP1^{+} puncta per cell (**b**,**g**,**l**,**q**,**v**), percentage of total LAMP1^{+} puncta also positive for ^{K}Dendra (**c**,**h**,**m**,**r**,**w**) and number of LAMP1^{+} puncta per cell (**d**,**i**,**n**,**s**,**x**). Means ± s.e.m. and individual values are shown. CMA score in hepatocytes (**e**), Kupffer cells (**j**) from young (3 m) and old (18–24 m) male and female mice, calculated from single-cell RNA-seq data from the Tabula Muris Senis dataset and in BAT (**o**), vWAT (**t**) and sWAT (**y**) from young (4–6 m) and old (24–28 m) male and female mice, calculated from RT–PCR analysis. Boxes: median and 25th and 75th percentiles. Whisker ends: 25th and 75th percentiles ± 1.5 times the IQR. Number of mice (cells (for liver and BAT) or fields (for vWAT and sWAT)) for YF, OF, YM and OM, respectively: **b**–**d**: 5 (200), 6 (240), 4 (160), 6 (250); **e**: 2 (536), 2 (517), 3 (1,768), 4 (108); **g**–**i**: 5 (200), 6 (240), 4 (170), 6 (240); **j**: 2 (13), 2 (246), 2 (614), 4 (1,673); **l**–**n**: 5 (135), 4 (140), 5 (148), 5 (142); **o**: 5, 4, 4, 4; **q**–**s**: 5 (121), 5 (92), 5 (126), 4 (108); **t**: 5, 9, 7, 9; **v**–**x**: 4 (90), 4 (90), 4 (96), 5 (120); **y**: 5, 7, 7 8. *P* values were calculated using two-way ANOVA with Bonferroni's multiple comparison test. Only significant comparisons are shown. Per-animal values are shown in Supplementary Fig. 3a–e. Number of cells counted per tissue and per animal are in Source Data Fig. 4. m, months; OF, old female; OM, old male; YF, young female; YM, young male.

https://doi.org/10.1038/s43587-024-00799-6

age in CMA in the cerebellum, we analyzed inhibitory (Calbindin$^+$ Purkinje cells) and excitatory (NeuN$^+$ granule cells) neurons from the same group of ^{KFERQ}Dendra mice (Fig. 3a–l; Calbindin and NeuN staining are shown in Extended Data Fig. 2a). Purkinje neurons exhibited approximately 50% loss of CMA activity with age in both male and female brains (Fig. 3a,b,i), whereas CMA activity in granule neurons remained unchanged with age, although it was significantly lower in males than in females even at young ages (Fig. 3e,f). The age changes and sex differences in CMA activity in cerebellum neurons both seem driven by overall changes in endolysosome number (Fig. 3d,h and Extended Data Fig. 2b), whereas the fraction of CMA-competent lysosomes remained unchanged (Fig. 3c,g). We did not find major changes in the transcription of CMA-related genes, which was only reduced with age in males in granule excitatory neurons in cerebellum (Fig. 3j,k and Extended Data Fig. 2c). Overall, Purkinje inhibitory neurons show one of the most marked declines in CMA activity with age among neurons and the only ones with similar magnitude in males and females (Fig. 3l compared to Fig. 1t).

Lastly, we analyzed neurons in a specialized component of the central nervous system—the retina. We compared CMA activity in two types of specialized retinal photoreceptor neurons, rods and cones, as CMA-mediated proteostasis is essential for retinal function, and pharmacological activation of CMA ameliorates retinal neurodegeneration in mice[29,41]. Rods, the major photoreceptors in nocturnal rodents, demonstrated age-dependent and sex-dependent differences in CMA (Fig. 3m,n), whereas overall CMA activity in cones did not differ among the groups (Fig. 3q,r and Extended Data Fig. 2d showing photoreceptor-specific labeling). CMA activity was higher in rods in young males than in females (Fig. 3m,n), but aging reversed these differences, leading to increased CMA in females and reduced CMA in males (Fig. 3m,n and Extended Data Fig. 2e). CMA activity in rods associated with differences in the fraction of CMA-competent lysosomes and in total endolysosome number (Fig. 3o,p). However, in cones, the increase with age in endolysosome number was neutralized by a reduction in CMA-competent lysosomes (Fig. 3s,t and Extended Data Fig. 2f), which could explain the absence of CMA changes in these neurons.

In summary, we found a more pronounced effect of aging on CMA in neurons than in astrocytes. The age-related decrease in CMA was more noticeable in hippocampus and Purkinje cerebellar cells and associated with a decrease either in the fraction of endolysosomes active for CMA or in total endolysosome content, depending on the cell type (Extended Data Fig. 2g,h). Overall, the contribution of transcriptional changes was more noticeable in males across all neuronal types (Extended Data Fig. 2h).

Cell-type-specific changes in CMA in aging metabolic tissues

The severe impact in overall organism metabolism observed upon selective blockage of CMA in hepatocytes and adipocytes[27,28,42] and the contribution of CMA to regulation of glucose and lipid metabolism made us next investigate cell-type-specific and sex-specific differences in CMA with age in the major metabolic organs.

We first analyzed CMA in the liver (Fig. 4a–j and Extended Data Fig. 3a–d) and found inverse sex differences in young mice, with males displaying higher CMA activity than females in hepatocytes and lower CMA activity in Kupffer cells (Fig. 4b,g; CD68 immunostaining was used to identify Kupffer cells in tissue sections as in Extended Data Fig. 3a). Cell-type-specific differences were also noticeable in the impact of aging, with reduced CMA activity in hepatocytes with age but not in Kupffer cells (Fig. 4b,g and Extended Data Fig. 3b). Aging changes in male hepatocytes associated with a decrease in endolysosome number, whereas, in females, only the fraction active for CMA was reduced (Fig. 4c,d and Extended Data Fig. 3b,c). Changes in the transcriptional CMA network may also contribute to reduced hepatocyte CMA with age in both males and females and to the slight, but significant, CMA increase in Kupffer cells in males (Fig. 4e,j and Extended Data Fig. 3d).

Considering the functional and regional differences of the brown adipose tissue (BAT) and white adipose tissue (WAT), we next analyzed CMA activity in BAT and in visceral (v) and subcutaneous (s) WAT (Fig. 4k–y and Extended Data Fig. 3e–g). Overall, sex differences in adipose tissue CMA were among the most pronounced across organs. Young males displayed more than 10-fold higher CMA activity in BAT than females, whereas CMA activity in both WAT depots was five-fold higher in young females than males (Fig. 4l,q,v). These sex differences coincided with corresponding changes in both the overall endolysosome number and fraction of CMA-active lysosomes (Fig. 4m,n,r,s,w,x and Extended Data Fig. 3e,f). Only in the sWAT, we noticed transcriptional differences in the CMA network that could explain the lower CMA activity in males, whereas, in the other fat depots, sex-related CMA differences may be mostly post-transcriptional (Fig. 4o,t,y and Extended Data Fig. 3g). Also unique to adipose tissue, CMA activity consistently increased with age in females across all three depots, whereas males exhibited either a decrease (BAT) or no change (vWAT and sWAT) (Fig. 4l,q,v and Extended Data Fig. 3e). Differences between males and females in age-related changes in CMA were not transcriptionally driven but, rather, associated with changes in endolysosomes (Fig. 4m–o,r–t,w–y and Extended Data Fig. 3f,g).

To characterize CMA changes in pancreas with age, we separately analyzed acinar cells (Fig. 5a–d and Extended Data Fig. 4a,b), responsible for the exocrine pancreatic function, and the endocrine pancreas β and α cells. Technical limitations prevented in situ detection of ^{K}Dendra signal in β and α cells, which was, instead, quantified upon parenchyma tissue disruption and isolation of islets of Langerhans from the same four groups of ^{KFERQ}Dendra mice (Fig. 5e–l and Extended Data Fig. 4a,b). Sex differences in CMA were noticeable only in acinar cells, which displayed slightly higher CMA activity in males (Fig. 5b), likely driven by an overall greater number of endolysosomes (Fig. 5d). CMA was reduced in acinar and β cells in both old males and old females (Fig. 5b,f,m), but no significant changes were observed in α cells (Fig. 5j). The decline in CMA with age in both sexes associated with reduced endolysosome number and lower percentage of CMA-active lysosomes (Fig. 5c,d,g,h,k,l and

Fig. 5 | Sex-specific and cell-type-specific changes in CMA activity with age in pancreas and skeletal muscle. a–**m**, CMA activity and endolysosomal changes in acinar cells in pancreas tissue sections (**a**–**d**), β cells (**e**–**h**) and α cells (**i**–**l**) in isolated islets of Langerhans and in myofibers of gastrocnemius skeletal muscles (**o**–**r**) from young (4–6 m) and old (24–28 m) female and male ^{KFERQ}Dendra mice. Confocal images (**a**,**e**,**i**,**q**) show the indicated cells stained for ^{K}Dendra and LAMP1. Scale bars, 10 µm (**a**,**q**) and 5 µm (**e**,**i**). Number of ^{K}Dendra$^+$LAMP1$^+$ puncta per cell (**b**,**f**,**j**) or normalized cell area (**o**), percentage of LAMP1$^+$ puncta positive for ^{K}Dendra (**c**,**g**,**k**,**p**) and number of LAMP1$^+$ puncta per cell (**d**,**h**,**l**) or normalized cell area (**r**). **m**, Quantification of changes in ^{K}Dendra$^+$LAMP1$^+$ puncta in the indicated pancreatic cells from old male and female mice relative to that in sex-matched young mice. Values are mean ± s.e.m. **n**,**s**, CMA score in pancreatic cells (**n**) from young (3 m) and old (18–24 m) male and female mice, calculated from single-cell RNA-seq data from the Tabula Muris Senis dataset or in skeletal muscle from young (4–6 m) and old (24–28 m) male and female mice (**s**) calculated by RT–PCR analysis. Boxes: median and 25th and 75th percentiles. Whisker ends: 25th and 75th percentiles ± 1.5 times the IQR. Number of mice (cells (for pancreas) or fields (for skeletal muscle)) for YF, OF, YM and OM, respectively: **b**–**d**,**m**: 6 (90), 6 (90), 9 (120), 7 (105); **f**–**h**,**m**: 2 (187), 2 (235), 2 (202), 3 (203); **j**–**l**,**m**: 3 (22), 3 (45), 3 (34), 3 (43); **n**: 2 (100), 1 (118), 2 (91), 3 (267) (acinar cells), 2 (281), 1 (142), 2 (241), 3 (678) (β cells), 2 (181), 1 (41), 2 (183), 3 (116) (α cells); **o**–**r**: 7 (140), 7 (140), 7 (140), 7 (140); **s**: 7, 6, 7, 6. *P* values were calculated using two-way ANOVA with Bonferroni's multiple comparison test. Only significant comparisons are marked. Lower magnification full-field images for **a**, **e**, **i** and **q** are shown in Supplementary Fig. 1m–p, and per-animal values are shown in Supplementary Fig. 3f–h for pancreatic cells and in Supplementary Fig. 4a for skeletal muscle fibers. Number of cells counted per tissue and per animal are in Source Data Fig. 5. m, months; OF, old female; OM, old male; YF, young female; YM, young male.

https://doi.org/10.1038/s43587-024-00799-6

Extended Data Fig. 4b) along with reduced transcriptional CMA score in the case of β cells in old males (Fig. 5n and Extended Data Fig. 4c).

Next, we analyzed CMA in gastrocnemius myofibers (Fig. 5o–s and Extended Data Fig. 4d,e). CMA activity was lower in young males than in young females, likely as a result of fewer endolysosomes (Fig. 5o–s). In contrast, a decrease in the fraction of lysosomes active for CMA may be behind the lower CMA activity with age observed in both male and female muscle myofibers (Fig. 5o–r and Extended Data Fig. 4d). A reduction in the transcriptional CMA score with age was noticeable only in males (Fig. 5s and Extended Data Fig. 4e).

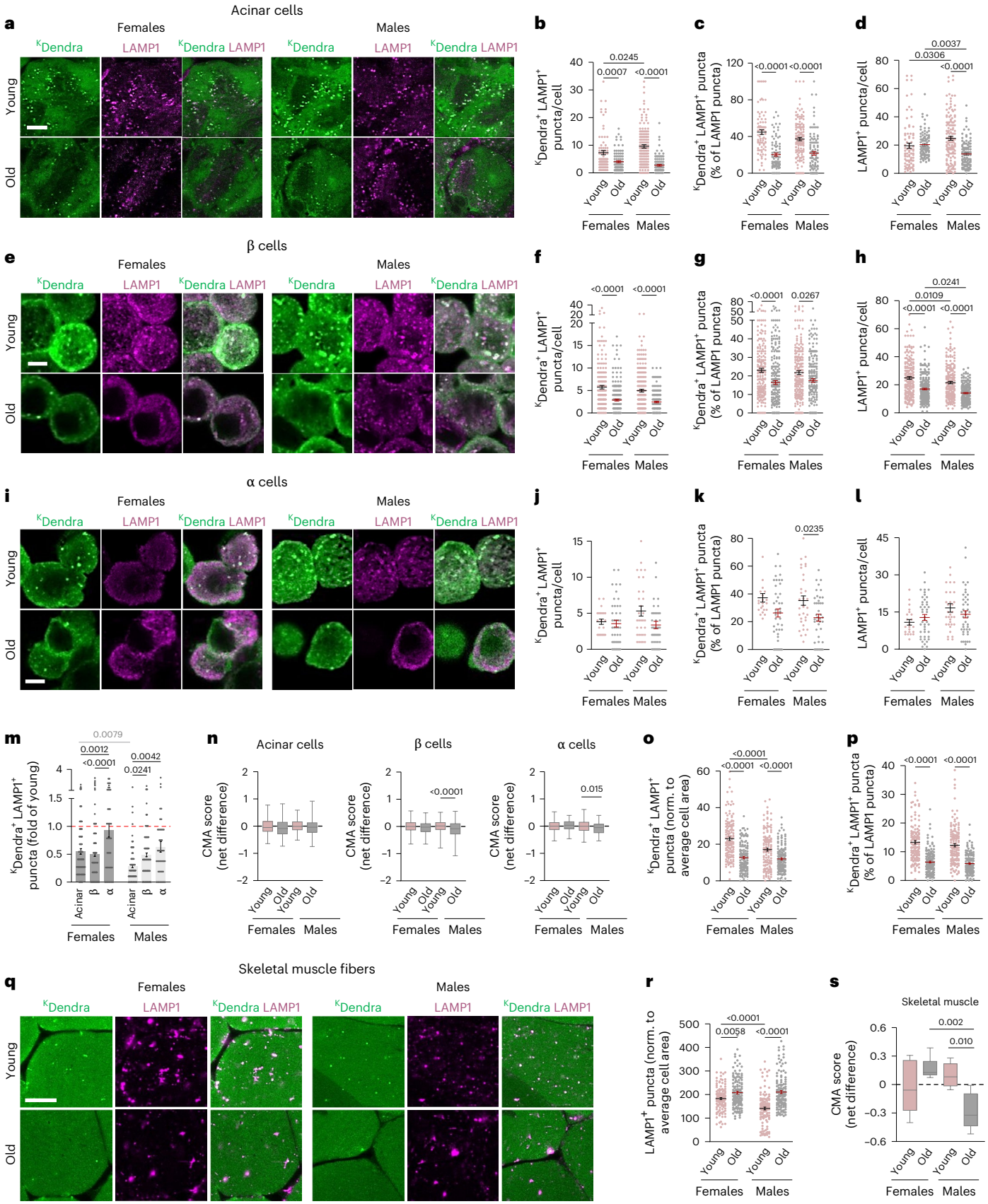

https://doi.org/10.1038/s43587-024-00799-6

In summary, most metabolically relevant organs display reduced CMA activity in aging, with the notable exception of the adipose depots, where CMA activity increases with age (Extended Data Fig. 4f,g). Adipose tissue, in particular the BAT, is also where we found more pronounced sex differences in CMA activity. Across-organ comparison revealed the highest levels of basal CMA activity in BAT and skeletal muscle, followed by the pancreas (Extended Data Fig. 4f,g). Mechanistically, age-related changes in CMA in females across most of these organs were likely driven by alterations in the fraction of endolysosomes allocated to this pathway, whereas males more frequently showed overall reduction in endolysosome number with age.

Sex-specific changes in CMA in kidney and heart in aging

We analyzed CMA in two additional major organs, kidney and heart, both highly prone to age-related fibrosis and inflammaging[43]. In kidney (Fig. 6a–n and Extended Data Fig. 5a–c), we observed sex differences in glomeruli, with higher CMA activity in young females compared to young males (Fig. 6a,b). Sex-dependent differences were also evident in aging kidneys, as females exhibited a more significant decline in CMA in glomeruli, while males exhibited a greater decline in tubules and collecting ducts (Fig. 6a,b,e,f,i,j,m). We observed a reduction with age in overall endolysosome number, and for tubules and collecting ducts, we also observed reduction in the fraction of CMA-competent lysosomes (Fig. 6c,d,g,h,k,l and Extended Data Fig. 5b). However, the transcriptional CMA score remained unchanged (Fig. 6n and Extended Data Fig. 5c), suggesting that CMA decline in aging kidneys may be mostly post-transcriptionally driven.

Lastly, we analyzed CMA activity in cardiomyocytes (Fig. 6o–s and Extended Data Fig. 5d–f) and observed no differences between young males and young females (Fig. 6p). CMA declined with age in cardiomyocytes in both males and females mostly due to fewer endolysosomes (Fig. 6o–r and Extended Data Fig. 5e), because, as in the case of kidneys, no significant changes were observed in transcriptional CMA score with age (Fig. 6s and Extended Data Fig. 5f).

Tissue-wide comparative changes in CMA activity with aging

To gain a more global view of systemic differences in CMA across organs, we compared CMA activity, proportion of CMA-competent lysosomes and total endolysosome number normalized by cell area to account for cell size differences (Fig. 7a,b and Extended Data Fig. 6). Uniform manifold approximation and projection (UMAP) graphs revealed the highest CMA activity by cell area in pancreas, kidneys, liver and certain brain regions (Fig. 7a). Differences were mostly driven by tubular and ductal cells in the case of the kidney, Kupffer cells in the liver and hippocampus and cerebellum neurons in the brain (Extended Data Fig. 6). These differences in CMA coincided with a higher endolysosomal content per cell area in the pancreas, liver and kidney, whereas brain cells exhibited a greater proportion of lysosomes engaged in CMA (Fig. 7a and Extended Data Fig. 6b). Cells in pancreas, kidneys, Kupffer cells and hippocampal neurons also had the most endolysosomes (Fig. 7a and Extended Data Fig. 6c). Transcriptionally, brain and, to some extent, heart showed the highest CMA score (Fig. 7b). Interestingly, despite male–female differences in tissue-specific CMA activity, relative CMA activity among cell types was largely consistent, except in BAT, which was among the tissues with highest CMA activity in males but not in females (Fig. 7a and Extended Data Fig. 6).

When comparing the effect of aging across tissues, with the exception of some specialized neurons and WAT, females displayed a generalized decrease in CMA, but the overall decrease in CMA with age was even more pronounced in males (CMA activity depicted as lower bubble size in Fig. 7c). Only Kupffer cells and hippocampal astrocytes exhibited an increase in CMA with aging in males (Fig. 7c). Males also exhibited greater decline in the total endolysosomal number, fraction of lysosomes active for CMA and the transcriptional CMA score across cell types and tissues (depicted as cooler bubble colors in Fig. 7c). In contrast, the impact of aging on both transcriptional and post-transcriptional changes in the number of endolysosomal compartments was very much cell type/tissue dependent in the case of females (Fig. 7c).

CMA, lysosome and macroautophagy changes with aging

Elucidating the molecular mechanisms behind CMA changes with aging requires further extensive characterization of the endolysosomal system for each cell type and tissue. To aid in this effort, in addition to changes in endolysosome number using L1 immunostaining, we examined expression of genes related to lysosomal function (hydrolases, membrane proteins and acidification-related components) and lysosomal biogenesis (Extended Data Fig. 7). Sexual dimorphism in expression of most lysosomal genes was evident in young males and young females across cell types (Extended Data Fig. 7a–e), but they did not always correlate with endolysosome number or CMA activity (Figs. 1–6). We noted marked transcriptional downregulation of lysosomal genes with age predominantly in males in almost all cell types analyzed (Extended Data Fig. 7a–e), aligning with reduced endolysosome numbers (Figs. 1–6). Except for some neuronal types and cardiomyocytes, old females were more likely to preserve the lysosomal transcriptional drive than old males (Extended Data Fig. 7a–e). These findings suggest that the reduced lysosome numbers with age in males may largely be due to transcriptional downregulation of lysosomal genes. A lysosomal score, based on the average expression of 53 lysosomal genes (Extended Data Fig. 6e), revealed cell-type-specific differences, even within the same tissue. This lysosomal score can be used to infer how transcriptional changes correlated with CMA activity, fraction of lysosomes active for CMA and the overall number of endolysosomes. For instance, in hippocampal neurons, the lysosomal score correlated with these three parameters, but this correlation was not observed in astrocytes or in neurons in other brain regions, such as cortex (Extended Data Fig. 7f).

Given the known interplay and compensation among different types of autophagy, we next analyzed the transcriptional profile of

Fig. 6 | Sex-specific and cell-type-specific changes in CMA activity with age in kidney and heart. a–**l** and **o**–**r**, CMA activity and endolysosomal changes in glomeruli (**a**–**d**), tubules (**e**–**h**) and collecting ducts (**i**–**l**) in kidney and cardiomyocytes in heart (**o**–**r**) from young (4–6 m) and old (24–28 m) female and male ^{KFERQ}Dendra mice. Representative confocal images show kidney glomeruli (**a**), tubules (**e**), collecting ducts (**i**) and cardiomyocytes (**o**) stained for ^{K}Dendra and LAMP1. Scale bars, 5 µm (**a**,**e**,**i**) and 10 µm (**o**). Quantification of ^{K}Dendra^{+}LAMP1^{+} puncta per cell (**b**,**f**,**j**) or per cell area (**p**), percentage of LAMP1^{+} puncta positive for ^{K}Dendra (**c**,**g**,**k**,**q**) and number of LAMP1^{+} puncta per cell (**d**,**h**,**l**) or per cell area (**r**). Individual values and means ± s.e.m. are shown. **m**, Quantification of changes in ^{K}Dendra^{+}LAMP1^{+} puncta in the indicated kidney cells from old male and female mice relative to that in sex-matched young mice. Values are mean ± s.e.m. **n**,**s**, CMA score in kidney cells (**n**) and cardiomyocytes (**s**) from young (3 m) and old (18–24 m) male and female mice, calculated from single-cell RNA-seq data from the Tabula Muris Senis dataset. Boxes: median and 25th and 75th percentiles. Whisker ends: 25th and 75th percentiles ± 1.5 times the IQR. Number of mice (glomeruli (**b**–**d**), cells (**f**–**h**,**j**–**l**) or fields (**p**–**r**)) for YF, OF, YM and OM, respectively: **b**–**d**,**m**: 5 (25), 5 (25), 4 (20), 5 (20); **f**–**h**,**m**: 5 (125), 5 (125), 4 (100), 5 (125); **j**–**l**,**m**: 5 (100), 5 (100), 4 (80), 5 (100); **n**: 2 (14), 1 (35), 4 (18), 6 (26) (glomerulus), 2 (3), 2 (85), 4 (43), 6 (262) (proximal tubules), 2 (69), 2 (243), 4 (110), 6 (180) (collecting ducts); **p**–**r**: 5 (226), 6 (261), 4 (182), 6 (243); **s**: 4 (113), 2 (65), 5 (92), 5 (280). *P* values were calculated using two-way ANOVA with Bonferroni's multiple comparison test. Only significant comparisons are marked. Lower magnification full-field images for **a**, **e**, **i** and **o** are shown in Supplementary Fig. 1q–t, and per-animal values are shown in Supplementary Fig. 4b–d for kidney cells and in Supplementary Fig. 4e for cardiomyocytes. Number of cells counted per tissue and per animal are in Source Data Fig. 6. m, months; OF, old female; OM, old male; YF, young female; YM, young male.

https://doi.org/10.1038/s43587-024-00799-6

effectors, receptors, activators and inhibitory macroautophagy genes in young and old male and female mice (Extended Data Fig. 8). A macroautophagy score was calculated upon conferring to each gene weight and directionality based on their effect on macroautophagy (Extended Data Fig. 6f). Changes in macroautophagy gene expression generally mirrored those of lysosome-related genes, with a similar sexual dimorphism across cell types in young mice and better preservation of expression of macroautophagy genes in old females than in old males,

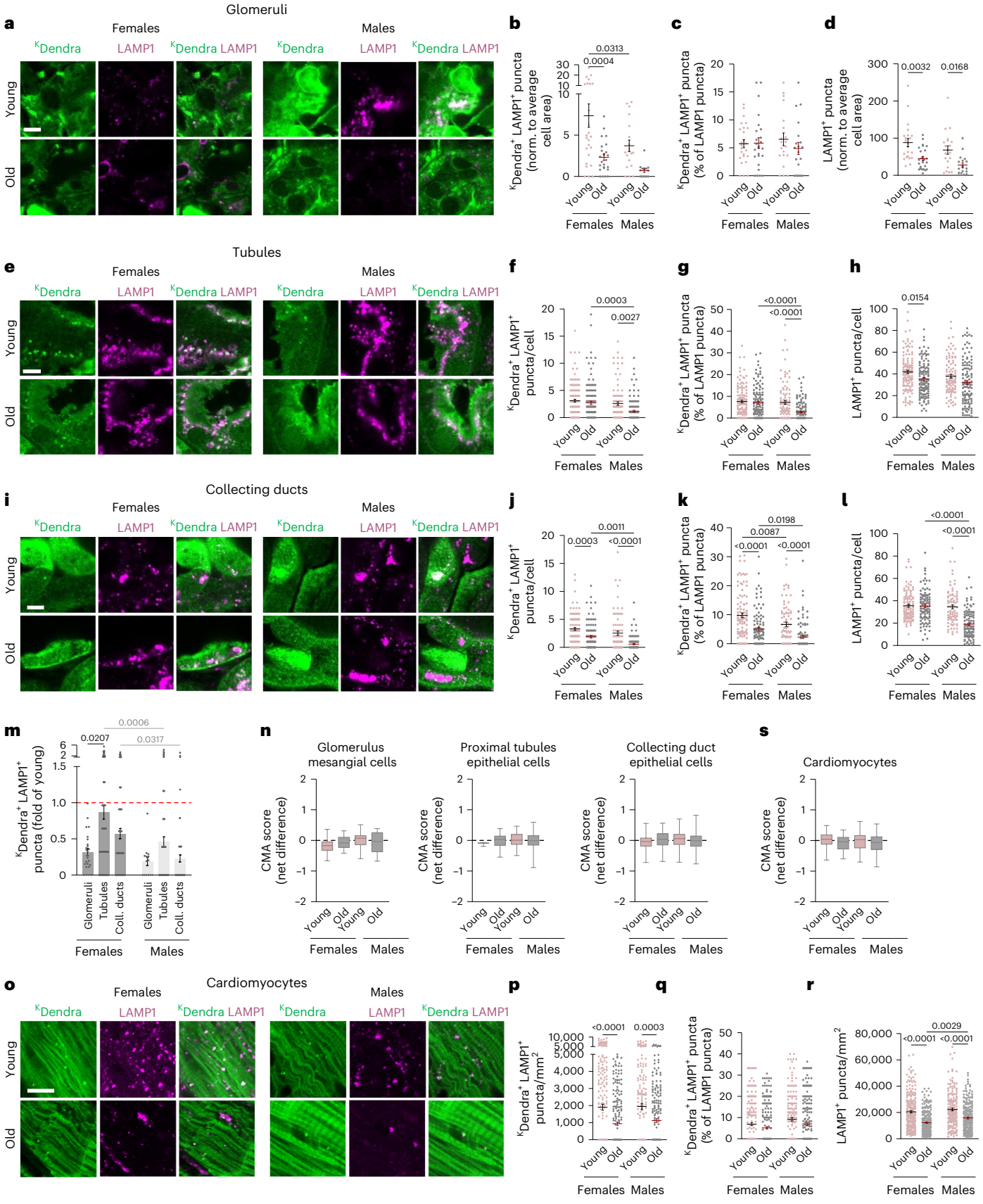

except for Kupffer cells, where macroautophagy genes were notably upregulated in old males (Extended Data Fig. 8).

Analysis of the members of the MiTF/TFE family of transcription factors, of which *Tfeb* and *Tfe3* are considered master regulators for both lysosomal biogenesis and macroautophagy (CLEAR network), revealed reduced expression with age in multiple tissues (Extended Data Fig. 6g–i). Upregulation of these genes may be behind the observed higher expression of lysosomal and macroautophagy genes in Kupffer cells in male mice and their sustained expression in the pancreas of old females. As expected, we found lower similarity between changes in MiTF family and CMA-related genes, because most of the key CMA components are not part of the CLEAR network.

Overall, transcriptional changes in lysosomal and macroautophagy genes were more similar to each other than to CMA-related genes, except in kidney cells and cardiomyocytes, where all three sets showed similar behavior (Extended Data Fig. 6d–f).

Discussion

In this work, we identified differences with sex in the tissue/cell-type-specific impact of aging on CMA and in the potential underlying mechanisms behind these changes. Our data support that CMA decreases with age in most of the tissues analyzed, and this decrease is more pronounced in males than in females.

Despite sex differences in life expectancy and disease propensity, the impact of sex on CMA activity remained unknown. This study identified sex differences in CMA in over half of the 25 tissues/cell types and organ regions analyzed, including organs such as adipose tissue where CMA was 4–8 times higher in female WAT than in male WAT but 20 times higher in male BAT compared to female BAT. It is interesting that several proteostasis genes, including *Lamp2*, are located on the X chromosome. Some genes can escape X inactivation and show higher expression in females[44]. Our analysis revealed that reduced expression of *Xist*, a key effector of X inactivation[45], correlated with higher transcriptional CMA score in several neuronal types, hepatocytes and kidney proximal tubule cells as well as with higher overall CMA activity in brain in old females (Extended Data Fig. 9a–h). Cell-type-specific reduction of *Xist* expression and subsequent higher expression of X chromosome genes may help preserve CMA in old females, especially in brain cells.

Hormonal regulation may also influence sex differences in age-related changes in CMA. Although our studies were performed with females in the same estrous stage, we attempted to correlate CMA activity with the expression of estrogen (*Esr1*, *Esr2* and *Gper1*) and testosterone (*Andr/Ar*) receptors in liver, adipose and skeletal muscle (Extended Data Fig. 10). Despite increase in expression of both types of receptors in the livers and skeletal muscles of old females compared to old males (Extended Data Fig. 10a–j, left panels), no consistent association between hormone receptor expression levels and CMA activity was observed across tissues, except for a negative correlation in young male BAT (Extended Data Fig. 10e–g, right panels). Future studies should explore whether lower overall sex hormone receptors expression/signaling in male BAT influences CMA activation in this organ.

CMA malfunction has been increasingly linked to various diseases[4,6,46], highlighting the importance of understanding age-related changes in this pathway. In the brain, experimental loss of neuronal CMA alone can trigger neuronal proteotoxicity and functional disruption, mirroring aging-related changes in this organ[47]. Although gene expression analysis provides insights into CMA, direct functional validation is necessary owing to the important post-transcriptional regulation of autophagy. For example, brain macroautophagy is transcriptionally downregulated with age[8,9], but it remains unclear if this leads to reduced macroautophagy[48].

Our findings reveal regional and cell-type-specific differences in basal brain CMA activity and aging effect, which may inform disease vulnerability. For example, the DG, highly sensitive to aging[49], showed the steepest decline in neuronal CMA activity with age, whereas neuronal CMA was higher in old mice in the entorhinal cortex, one of the earliest regions affected in AD[50,51]. These findings may point out differences in vulnerability of entorhinal cortex neurons to aging versus AD-related proteotoxicity[52]. It is possible that this upregulation of CMA with age makes entorhinal cortex neurons more dependent on CMA and, consequently, more vulnerable to the previously described blockage of CMA by pathogenic proteins such as tau[22,53]. In cerebellum, CMA declines in Purkinje but not granule neurons, aligning with greater Purkinje neuron loss with age[54,55]. In contrast, we observed preservation of CMA activity with age in photoreceptors of the retina, in agreement with the reported CMA upregulation to compensate for macroautophagy loss[41]. The increase in rod CMA activity with aging, specific to females, may be neuroprotective, as pharmacological upregulation of CMA ameliorates retinal degeneration in a retinitis pigmentosa mouse model[29]. Further research is needed to determine whether the decline in CMA in male rods with age contributes to their greater susceptibility to degeneration[56,57] and higher prevalence of macular degeneration in males[58].

Astrocytic CMA has garnered less attention than neuronal CMA, but it is increasingly recognized as important in brain injury[59,60] and neurodegenerative conditions[61]. Age-related changes in astrocytes are subtler and sometimes opposite to neuronal changes (that is, reduced neuronal CMA in hippocampal CA1 of old males coincides with increased astrocytic CMA, whereas the reverse is observed in entorhinal cortex). Future studies on autonomous and non-cell-autonomous regulation of CMA in brain may be able to explain these cell-type-specific different behaviors. Mechanistically, astrocytes, despite having fewer endolysosomes, show a higher proportion of lysosomes involved in CMA, which further increases with age. An exception was astrocytes in the entorhinal cortex, a region severely affected in AD[62], where CMA activity and CMA-active lysosome fraction sharply declined with age (almost 10-fold in males). This may indicate that astrocytes rely heavily on lysosome numbers to maintain proper CMA function.

In metabolic organs, the age-related decline in liver CMA is primarily driven by hepatocytes, because Kupffer cells maintain or even upregulate CMA in old mice. Preserved CMA in Kupffer cells could be related to their activation state, as number and size of Kupffer cells and pro-inflammatory macrophages increases with age and in age-related

Fig. 7 | Tissue-wide comparison of sex-specific and cell-type-specific changes in CMA activity with aging. a, UMAPs generated using each cell quantified in Figs. 1–6 after correcting for differences in cell area (all values calculated as puncta per mm^2 of cell area). The two-dimensional distribution in young female and young male ^{KFERQ}Dendra mice was determined based on its identity, ^{K}Dendra^{+}LAMP1^{+} puncta (CMA activity), ^{K}Dendra^{+}LAMP1^{+}/LAMP1^{+} (% of CMA-active lysosomes) and LAMP1^{+} puncta (endolysosomal number) separately in females (left) and males (right). Distribution of organ type is shown in the top panels. **b**, UMAP distribution and comparison of transcriptional CMA score across the organs, calculated from single-cell RNA-seq data from the Tabula Muris Senis dataset. Distribution of tissues (top panel) and their respective CMA scores (bottom panel) in all the cells obtained from young female and young male mice. **c**, Bubble plots to illustrate changes in CMA activity *z*-score (^{K}Dendra^{+}LAMP1^{+} puncta, balloon size) compared to fraction of CMA-active lysosome *z*-score (^{K}Dendra^{+}LAMP1^{+} puncta as a percentage of LAMP1^{+} puncta, left panel, balloon color), endolysosome number *z*-score (LAMP1^{+} puncta, middle panel, balloon color) and CMA transcriptional *z*-score (CMA score, right panel, balloon color) in all the indicated cell types and tissues from young (Y) and old (O) male and female mice. ^{K}Dendra^{+}LAMP1^{+} puncta, ^{K}Dendra^{+}LAMP1^{+}/LAMP1^{+} (%), LAMP1^{+} puncta and transcriptional CMA scores were calculated as *z*-score in young females and young males for each cell type separately. CB, cerebellum; EC, entorhinal cortex; SC, somatosensory cortex; lys., lysosome; transcr., transcriptional.

https://doi.org/10.1038/s43587-024-00799-6

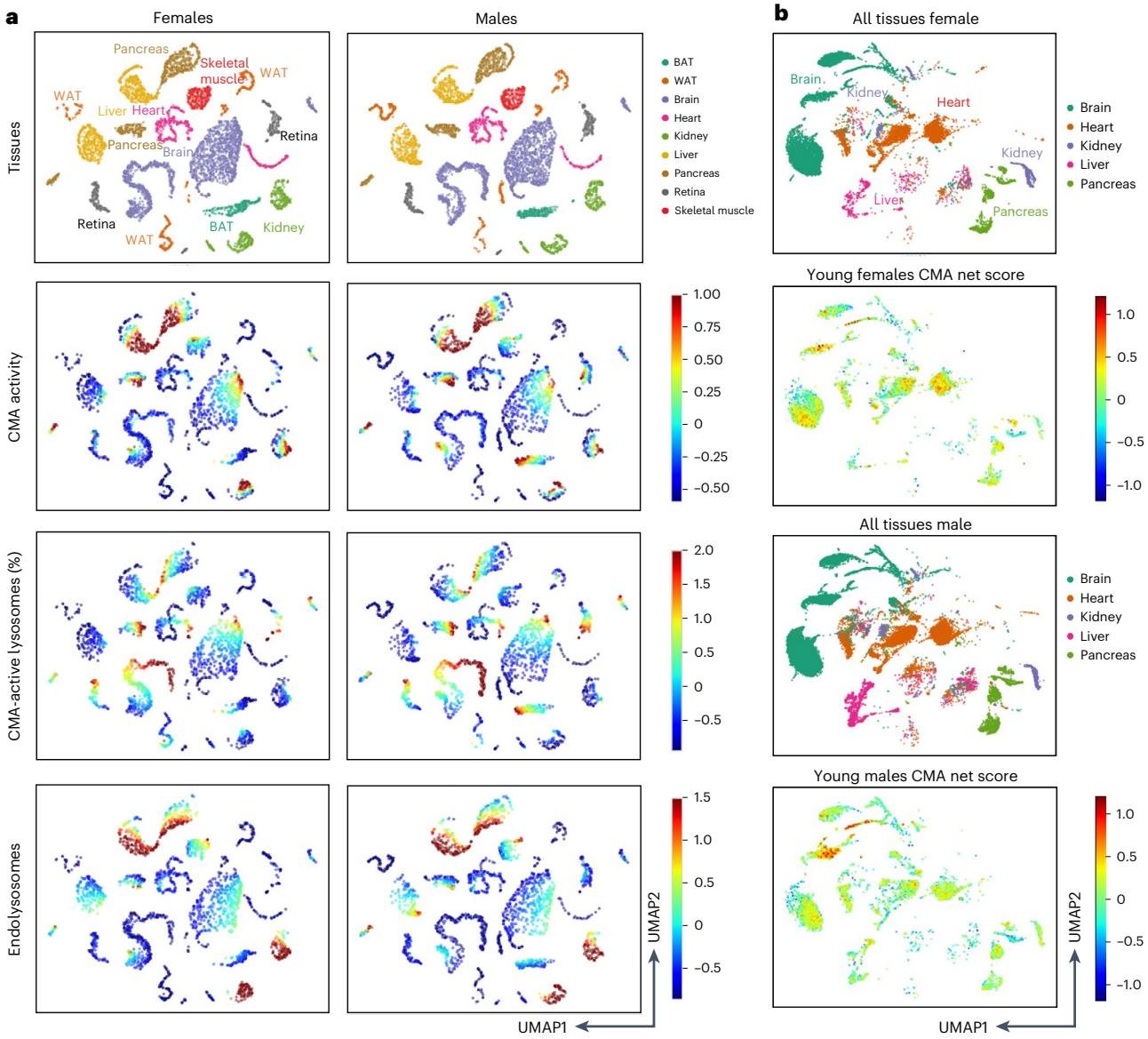

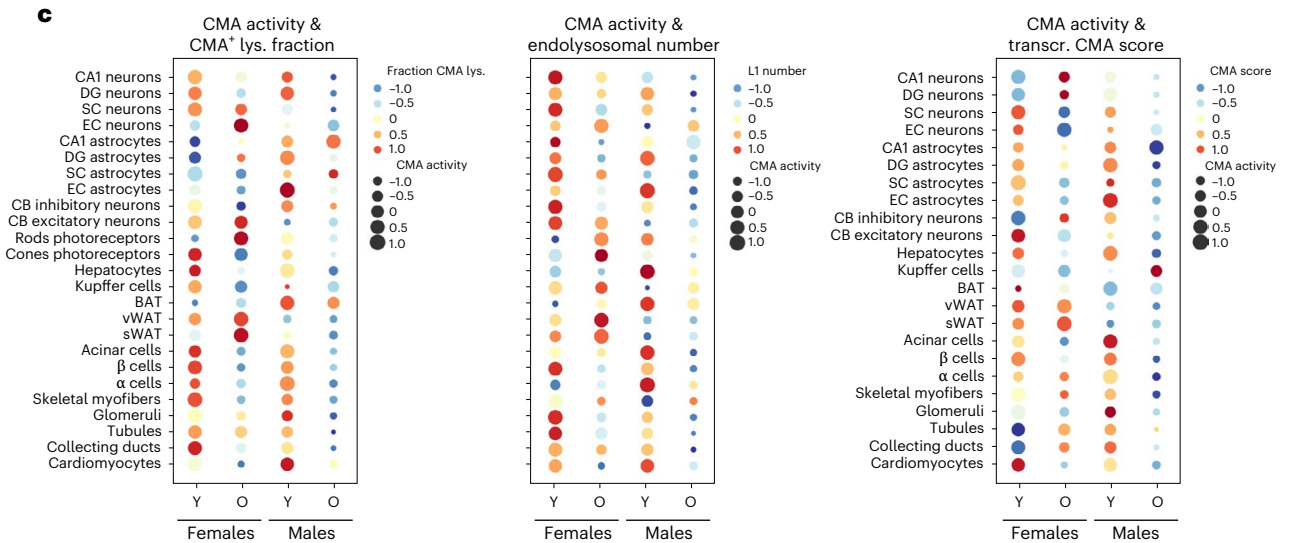

liver diseases[63,64]. CMA also declines with age in pancreas, kidney, heart and skeletal muscle, largely independent of sex. Interestingly, the exocrine pancreas and kidney are among the organs with higher CMA and macroautophagy activities[65], suggesting that they may require robust autophagy for protein control of their very active secretome[66]. Declining CMA in acinar cells, especially in males, might contribute to higher male propensity to pancreatic disorders, such as chronic pancreatitis[67]. Quality control of the secretome by CMA may also be crucial in pancreatic β cells, responsible for insulin secretion. Although CMA analysis in β cells could be performed only after islet of Langerhans isolation, the marked reduction in CMA activity and transcriptional score in β cells from old mice highlights the need for future studies on the impact of CMA failure on β cell function. In the kidney, CMA decreases with age in female glomeruli and in male ducts and tubules. Although macroautophagy remains unchanged with age in glomeruli, its increase in kidney epithelial cells in proximal tubes may be a response to CMA loss[12], and, thus, the worsening of kidney disease and fibrosis with aging, attributed to persistence of macroautophagy[13,14], could be a consequence of CMA decline.

Adipose tissues exhibit the most pronounced sexual dimorphism in the impact of aging on CMA. In females, CMA increases with age in all adipose tissues, whereas it remains unchanged or decreases in males. CMA upregulation may compensate for the faster decline in other autophagy types, similar to the increase in mitophagy observed with age in several organs despite reduced macroautophagy[68]. It may also serve as a protective response to age-related metabolic changes, possibly explaining the higher incidence of obesity-related adipocyte hyperplasia in males[69]. Lastly, CMA upregulation could also contribute to adipose tissue malfunction, as seen for macroautophagy in the aging WAT[11] where it causes fat atrophy and lipid accumulation[11]. Studies are needed to clarify whether increased CMA in adipocytes is protective or detrimental in aging.

Mechanistically, males displayed greater transcriptional reduction in CMA, macroautophagy and lysosomal components with age in most of the cell types, which may contribute to their greater vulnerability to loss of CMA activity in aging. In contrast, females were more likely to preserve or increase gene expression of autophagy components with aging. The contribution of inter-individual differences in X chromosome inactivation to the preserved CMA transcriptional profile in old females requires future investigation.

This study highlights the vulnerability of multiple tissues and cell types to age-related CMA changes, the sex-imposed differences in these changes and the cell-type-specific mechanisms contributing to CMA loss, including transcriptional downregulation, reduced lysosomal numbers and fewer lysosomes allocated to CMA. Similar analysis in all cell types in an organism is beyond this study's scope, but it would be interesting to see the contribution of CMA in the immune system, given its role in inter-organ communication and reported decrease in CMA activity with age in immune cells, such as T cells[20,26]. All CMA measurements in this study rely on the fluorescent reporter and were done under basal conditions. Future development of complementary methods for CMA analysis in individual cell types will be important to validate these findings and determine if the observed changes in CMA display some level of context dependence. Although we used a single mouse strain, the findings are likely generalizable, as similar CMA reduction in liver has been observed in at least three different mouse strains and in rats.

The sex-specific and tissue-specific differences in the mechanism behind CMA malfunctioning in aging underscore the need for targeted and combinatorial approaches in developing gerotherapeutic interventions based on CMA regulation.

Methods

Mice

KFERQ-Dendra2 transgenic male and female mice in a C57BL/6J background at 4–6 months and 24–28 months of age were used in this work. KFERQ-PS-Dendra2 mice were generated by donor egg injection in wild-type mice using the pRP.ExSi plasmid backbone with the insert coding for 11 amino acids, including the KFERQ sequence of RNase A in frame with the sequence of Dendra2 under the hybrid promoter CAGG[32]. Congenic C57BL/6J background KFERQ-Dendra mice were created by backcrossing for more than 10 generations the original FVB KFERQ-Dendra mice[32] with C57BL/6J wild-type mice (The Jackson Laboratory, strain no. 000664). Mice were housed in ventilated cages with no more than five mice per cage on a 12-h light/dark cycle at 23 °C and 40–60% humidity with ad libitum access to water and standard rodent chow in our pathogen-free barrier facility along with sentinel cages. In all experiments, to detect baseline CMA activity, mice were fed during the dark cycle, and organs were harvested 2–4 h after the beginning of the light cycle (to avoid upregulation of CMA by starvation, which will not occur until 10 h of food deprivation)[32,36,70]. Mice were euthanized between 2 h and 4 h of the starting of the light cycle to reduce circadian variability (mice in this colony consume most of the food during the first 4 h and last 3 h of the dark cycle). All mouse procedures, including genotyping, breeding, housing and euthanasia, were under an animal study protocol approved by the Institutional Animal Care and Use Committee of Albert Einstein College of Medicine.

Reagents

Sources of antibodies, including dilutions and other reagents, are indicated in Supplementary Table 2. We provided catalog numbers for all the commercial antibodies. All the antibodies used are commercial, were chosen based on extensive use in the literature and were validated using positive and negative controls by immunoblot and immunostaining.

Tissue processing

Mice were anesthetized with 4% isoflurane and subjected to trans-cardiac perfusion with 0.9% NaCl for 3–5 min. Brain, retina, liver, adipose tissues, pancreas, gastrocnemius muscles, kidneys and heart were collected and fixed with zinc formalin (Z-FIX; Anatech Ltd., 171) for 24 h and then stored in 0.1% (w/v) sodium azide in PBS and kept at 4 °C until use. Tissues were sectioned with either a Leica 1950 cryostat (brain, retina and gastrocnemius muscles) or a Leica VT 1000 S vibratome (heart, pancreas, BAT, liver and kidney). Before sectioning, samples were preserved in 30% sucrose (in 1× PBS) for at least 36 h for cryoprotection. Samples were subsequently frozen in Tissue-Tek optimum cutting temperature (O.C.T.) compound (Sakura) with dry ice. From brain samples, 40-µm free-floating sections were collected in stereological manner in 24-well plates. From gastrocnemius muscles and retina samples, 12-µm sections were collected directly on pre-treated slides, respectively. Heart, pancreas, BAT, liver and kidney were sectioned 40 µm thick and collected free floating in 24-well plates. For vWAT and sWAT, approximately 2-mm^3 sections of fat depots after fixation were collected in 24-well plates. In the case of the pancreas, islets of Langerhans were isolated after collagenase P (Roche) injection through the pancreatic duct as described previously[71]. The islets were washed repeatedly with Hanks FBS, and a density gradient was performed with Histopaque-1077 (Sigma-Aldrich). Islets were collected with a pipette, washed repeatedly with Hanks and placed in a Petri dish with RPMI 1640 medium (Gibco/Invitrogen) supplemented with 10% FBS and 1% penicillin–streptomycin. The next day, the islets were handpicked and placed on coverslips for subsequent staining for α and β cells.

Immunofluorescence

Tissue sections were permeabilized and blocked with 0.3% Triton X-100, 2% BSA and 10% goat or horse serum for 2 h at room temperature and then incubated with primary antibodies (Supplementary Table 2) in the same blocking solution at 4 °C overnight. After brief washing with PBS (for 5 min, three times), the sections were incubated with Hoechst 33342 (Invitrogen, 1:2,000) to highlight nuclei and secondary

antibodies (Supplementary Table 2) in blocking solution for 2 h at room temperature. After brief washing with PBS (for 5 min, three times), the sections were mounted on glass slides with ProLong antifade reagents (Thermo Fisher Scientific). Images were acquired with a Leica TCS SP8 confocal microscope using ×40 or ×63 objective and 1.4 numerical aperture and Leica LAS AF Lite software (version 4.0). Images were prepared, and channels were given pseudo colors (in some instances) and thresholded using ImageJ/Fiji (National Institutes of Health (NIH))[72].

RT–qPCR

RT–qPCR was performed in gastrocnemius skeletal muscles and adipose tissues to calculate CMA score as Tabula Muris Senis database lacked skeletal myofibers and adipocytes. RT–PCR was also performed in liver, BAT and gastrocnemius skeletal muscles to quantify hormone receptor levels. Total RNA was isolated with TRIzol (Invitrogen) for tissues (whole eWAT fat pad, sWAT, BAT, liver and gastrocnemius muscles) and by using an RNeasy Plus Mini Kit (Qiagen) according to the manufacturer's instructions. Genomic DNA was excluded using a gDNA eliminator spin column. Total RNA (1 µg) was reverse transcribed into cDNA using SuperScript III (Invitrogen), and RT–qPCR analyses were performed using Power SYBR Green PCR Master Mix (Applied Biosystems) on a StepOne Plus Real-Time PCR System (Applied Biosystems). Normalization of expression was performed using the mean of four housekeeping genes: TATA-binding protein (Tbp), β-actin (Actb), β2 microglobulin (B2m) and hypoxanthine phosphoribosyltransferase 1 (Hprt1). The mRNA expression in control samples (young females) was represented as 1, and mRNA expression in experimental samples was represented as fold change compared to expression in controls. The primers used are listed in Supplementary Table 3.

CMA score analysis with Tabula Muris Senis

The CMA score is a mathematical calculation that infers the CMA activity status[22]. It is based on the gene expression levels of a network of proteins that are directly involved in or regulate CMA (positively or negatively). CMA scores were calculated per cell type and tissue as previously described[22] using a single-cell RNA sequencing (RNA-seq) dataset available and annotated in the repositories of the Tabula Muris Senis consortium[35] (https://cellxgene.cziscience.com/collections/0b9d8a04-bb9d-44da-aa27-705bb65b54eb). Brain, heart, kidney and pancreas information was extracted from Tabula Muris Senis from Smart-seq2 sequencing system data, because of the better detection of genes in this system compared to 10× 3′ v2 sequencing. Liver data were calculated from Tabula Muris Senis using both Smart-seq2 (for combining all Tabula Muris Senis tissues in UMAP; Fig. 7b) due to representative purposes and 10× 3′ v2 sequencing system data (for Figs. 4e,j and 7c and Extended Data Figs. 3d, 4g, 6d–i, 7b, 8b and 9d) due to unavailability of young female Kupffer cell information in the Smart-seq2 system. Both Smart-seq2 and 10× 3′ v2 showed similar results for CMA score in liver. All the code required to reproduce the CMA score calculations is available from https://amsegura.github.io/Khawaja_et_al_2024/.

Statistics and reproducibility

Quantitative data are presented as individual data and as the mean ± s.e.m. The transcriptomic analysis data are presented as box plots showing median and interquartile range (IQR), with the upper and lower whiskers (whisker ends) indicating 25th and 75th percentiles ± 1.5 times the IQR. Power analysis was used to determine the number of animals required for each cell type/organ analysis based on the previous biochemical and histological differences that we found when analyzing basal CMA activity and response to stress in liver, heart and brain in vivo using the same reporter mouse model[32]. With the calculated sample size and a two-sided type 1 error rate of 5%, the analysis was predicted to have more than 80% power to detect effects of more than 1.5 in the parameters examined. None of the animals or data were excluded from the study. The experimental design does not allow for randomization, as age and sex were variables in the study. The investigators were not blinded during the dissection of the tissues, but batches of images were acquired using blinded observers, and information on sex and age group was then lifted for plotting and statistical analysis. Each animal was analyzed separately, and at least three tissue slices were imaged from each organ for replication purposes. Experiments were performed in animals collected at independent days to confirm reproducibility of the findings.

Tissue image quantification was performed by counting puncta particles from $n = 25–400$ cells or fields from approximately 3–8 mice per group using NIH ImageJ/Fiji software for imaging and DiAna plugin (version 1.53)[72,73] for quantification. The cell selection for quantification of puncta and the quantification of puncta were performed in a blinded fashion. In brief, the number of ^{K}Dendra^{+}LAMP1^{+} puncta in all cell types was quantified by drawing region of interests (ROIs) using the image channel containing cell type marker or LAMP1 (for tissues where the cell type marker was not used). This allowed for unbiased selection of cells for quantification that was performed automatically using DiAna software with same threshold selected for all the ROIs in the four groups (young female, old female, young male and old male) for each cell type. A batch analysis was then performed that generated the results at the same time for all the quantified cells in all the four groups. The number of ^{K}Dendra^{+}LAMP1^{+} per cell was used for quantification of CMA in brain, retina, liver, adipose tissues, pancreas, skeletal muscles and kidneys. In syncytial multinucleate cells such as skeletal muscle fibers and cardiomyocytes in the heart, and in cells where cell boundaries were not easily identified (that is, glomeruli), CMA was quantified as the number of ^{K}Dendra^{+}LAMP1^{+} per cell area; regions lacking LAMP1^{+} were not considered; and outliers were removed. Cell area correction was also used for all tissues for the comparative analysis of CMA activity across organs. For each cell type except isolated β and α cells of pancreas, CMA activity was analyzed in situ in independent mice per group. Individual cells were counted for each experiment to gain information of intra-tissue heterogeneity, and variance was calculated (Supplementary Table 1). Number of cells quantified per cell type in each mouse and number of mice per group/experiment are summarized in Source Data. Outliers were identified using the ROUT method.

All CMA score quantifications using Tabula Muris Senis repository were done in Python version 3.8.16 (ref. 74). The following packages were used for this purpose: matplotlib version 3.5.1; numpy version 1.24.4; pandas version 1.5.3; scanpy version 1.9.1; and seaborn version 0.12.2. UMAP was performed on Tabula Muris Senis and immunofluorescence quantifications for representation purposes only. In the case of Tabula Muris Senis data, UMAP calculation from the scanpy package was used. To calculate the UMAP dimensions on immunofluorescence quantifications, scikit-learn version 1.0.2 and umap-learn version 0.5.3 were used. For UMAPs, data were normalized by area for each cell for the calculations, including ^{K}Dendra^{+}LAMP1^{+} (CMA activity), percentage of CMA-active from total LAMP1^{+} puncta and LAMP1^{+} puncta (endolysosome quantification). In addition, each cell was given a value of 1 for the antibody used for its identification (for example, GFAP for astrocytes) and 0 for the rest of the antibodies. For those cell types that did not require antibody staining for identification, a value of 1 was given in a category created for them with 0 for the rest of the antibodies or cell markers. Thus, each cell type was identified either with an antibody signal or a cell type marker. The data were standardized using StandardScaler from scikit-learn before applying UMAP calculation. The normalized data were provided for the UMAP quantification, using n_neighbors = 200, min_dist = 0.5, spread = 0.5 and metric = 'Chebyshev' as parameters. For UMAP representations colored by CMA features (for example, CMA score or CMA activity), the range of the color bars was adjusted in their upper part to avoid outliers' disturbances in the color pattern. Balloon plots were done with data from immunofluorescence analysis and from the analyzed

single-cell RNA datasets. For each of the parameters (^{K}Dendra^{+}LAMP1^{+} (CMA activity); percentage of CMA-active from total LAMP1^{+} puncta; LAMP1^{+} puncta; and CMA score calculated on transcriptomic data), the mean value for young and old females and males was calculated. Those four values were normalized using a *z*-score calculation per cell type, using the normalized values for this summary representation.

Graphical plots were created and statistical analysis was performed using GraphPad Prism 9.0 (GraphPad Software). Statistical significance was assessed with two-tailed unpaired Student's *t*-test for two groups, two-way ANOVA followed by Bonferroni's multiple comparisons test for multiple groups or simple linear regression with exact *P* values or $^{*}P < 0.05$, $^{**}P < 0.01$, $^{***}P < 0.001$ and $^{****}P < 0.0001$ marked in the graphs and non-significant comparisons ($P > 0.05$) not marked. A cutoff of R^2 between 0.1 and 0.5 (when $P < 0.05$) or R^2 greater than 0.5 was used to denote significant correlations. A linear regression line was shown in figures with significant correlations.

Additional statistical analyses were also performed to account for potential correlation in data from cells from the same animal and to address non-normality and zero/one inflation in some of the data distributions[75]. Mixed effects negative binomial regression models were fit to handle the skewed and correlated count data from measures of ^{K}Dendra^{+}LAMP1^{+} and LAMP1^{+} puncta per cell in the cell types of brain, retina, liver, BAT, pancreas, kidney tubules and kidney collecting ducts. Two-part mixed effects gamma regression models, in which the first part models the probability that a zero versus non-zero value is observed, and the second part models the strictly non-zero positive data[75,76], were fit to analyze the zero-inflated correlated continuous data from those organs in which ^{K}Dendra^{+}LAMP1^{+} and LAMP1^{+} puncta were analyzed per area, which include vWAT, sWAT, skeletal myofibers, kidney glomeruli and cardiomyocytes. Two-part mixed effects beta regression models were fit to the zero/one-inflated correlated data on percentage of total LAMP1^{+} puncta also positive for ^{K}Dendra in all analyzed cell types. Pairwise comparisons were adjusted for multiple comparisons using Bonferroni's method, and results from these comparisons are shown in each of the graphs of Supplementary Figs. 2–4. The data per mouse and detailed results from these statistical analyses are also shown in Supplementary Data Files 1–3.

Reporting summary

Further information on research design is available in the Nature Portfolio Reporting Summary linked to this article.

Data availability

There are no restrictions on data availability in this paper. The single-cell RNA-seq dataset used in this work is available and annotated in the repositories of the Tabula Muris Senis consortium[35] (https://cellxgene.cziscience.com/collections/0b9d8a04-bb9d-44da-aa27-705bb65b54eb). All the information is included in the paper. All main and extended data figures have associated Source Data that is provided as an Excel worksheet organized by figures, and it includes statistics along with exact *P* values.

Code availability

All the codes required to reproduce the CMA score calculations and interactive version of UMAP representations in this paper are available from https://amsegura.github.io/Khawaja_et_al_2024/.

References

1. Lopez-Otin, C., Blasco, M. A., Partridge, L., Serrano, M. & Kroemer, G. The hallmarks of aging. *Cell* **153**, 1194–1217 (2013).
2. Brandvold, K. R. & Morimoto, R. I. The chemical biology of molecular chaperones—implications for modulation of proteostasis. *J. Mol. Biol.* **427**, 2931–2947 (2015).
3. Nieto-Torres, J. L. & Hansen, M. Macroautophagy and aging: the impact of cellular recycling on health and longevity. *Mol. Aspects Med.* **82**, 101020 (2021).
4. Kaushik, S. et al. Autophagy and the hallmarks of aging. *Ageing Res. Rev.* **72**, 101468 (2021).
5. Yamamoto, H., Zhang, S. & Mizushima, N. Autophagy genes in biology and disease. *Nat. Rev. Genet.* **24**, 382–400 (2023).
6. Kaushik, S. & Cuervo, A. M. The coming of age of chaperone-mediated autophagy. *Trends Cell Biol.* **19**, 365–381 (2018).
7. Aman, Y. et al. Autophagy in healthy aging and disease. *Nat. Aging* **1**, 634–650 (2021).
8. Ximerakis, M. et al. Single-cell transcriptomic profiling of the aging mouse brain. *Nat. Neurosci.* **22**, 1696–1708 (2019).
9. Lipinski, M. M. et al. Genome-wide analysis reveals mechanisms modulating autophagy in normal brain aging and in Alzheimer's disease. *Proc. Natl Acad. Sci. USA* **107**, 14164–14169 (2010).
10. Bejarano, E. et al. Defective recruitment of motor proteins to autophagic compartments contributes to autophagic failure in aging. *Aging Cell* **17**, e12777 (2018).
11. Yamamuro, T. et al. Age-dependent loss of adipose Rubicon promotes metabolic disorders via excess autophagy. *Nat. Commun.* **11**, 4150 (2020).
12. Yamamoto, T. et al. Time-dependent dysregulation of autophagy: implications in aging and mitochondrial homeostasis in the kidney proximal tubule. *Autophagy* **12**, 801–813 (2016).
13. Livingston, M. J. et al. Persistent activation of autophagy in kidney tubular cells promotes renal interstitial fibrosis during unilateral ureteral obstruction. *Autophagy* **12**, 976–998 (2016).
14. Tang, C., Livingston, M. J., Liu, Z. & Dong, Z. Autophagy in kidney homeostasis and disease. *Nat. Rev. Nephrol.* **16**, 489–508 (2020).
15. Sun, N. et al. Measuring in vivo mitophagy. *Mol. Cell* **60**, 685–696 (2015).
16. Krause, G. J. et al. Reduced endosomal microautophagy activity in aging associates with enhanced exocyst-mediated protein secretion. *Aging Cell* **21**, e13713 (2022).
17. Cuervo, A. M. & Dice, J. F. Age-related decline in chaperone-mediated autophagy. *J. Biol. Chem.* **275**, 31505–31513 (2000).
18. Kiffin, R. et al. Altered dynamics of the lysosomal receptor for chaperone-mediated autophagy with age. *J. Cell Sci.* **120**, 782–791 (2007).
19. Dong, S. et al. Chaperone-mediated autophagy sustains haematopoietic stem-cell function. *Nature* **591**, 117–123 (2021).
20. Valdor, R. et al. Chaperone-mediated autophagy regulates T cell responses through targeted degradation of negative regulators of T cell activation. *Nat. Immunol.* **15**, 1046–1054 (2014).
21. Kaushik, S., Massey, A. C. & Cuervo, A. M. Lysosome membrane lipid microdomains: novel regulators of chaperone-mediated autophagy. *EMBO J.* **25**, 3921–3933 (2006).
22. Bourdenx, M. et al. Chaperone-mediated autophagy prevents collapse of the neuronal metastable proteome. *Cell* **184**, 2696–2714 (2021).
23. Cuervo, A. M., Stefanis, L., Fredenburg, R., Lansbury, P. T. & Sulzer, D. Impaired degradation of mutant α-synuclein by chaperone-mediated autophagy. *Science* **305**, 1292–1295 (2004).
24. Orenstein, S. J. et al. Interplay of LRRK2 with chaperone-mediated autophagy. *Nat. Neurosci.* **16**, 394–406 (2013).
25. Sooparb, S., Price, S. R., Shaoguang, J. & Franch, H. A. Suppression of chaperone-mediated autophagy in the renal cortex during acute diabetes mellitus. *Kidney Int.* **65**, 2135–2144 (2004).
26. Madrigal-Matute, J. et al. Protective role of chaperone-mediated autophagy against atherosclerosis. *Proc. Natl Acad. Sci. USA* **119**, e2121133119 (2022).

27. Schneider, J. L., Suh, Y. & Cuervo, A. M. Deficient chaperone-mediated autophagy in liver leads to metabolic dysregulation. *Cell Metab.* **20**, 417–432 (2014).
28. Kaushik, S. et al. Chaperone-mediated autophagy regulates adipocyte differentiation. *Sci. Adv.* **8**, eabq2733 (2022).
29. Gomez-Sintes, R. et al. Targeting retinoic acid receptor alpha-corepressor interaction activates chaperone-mediated autophagy and protects against retinal degeneration. *Nat. Commun.* **13**, 4220 (2022).
30. Zhang, C. & Cuervo, A. M. Restoration of chaperone-mediated autophagy in aging liver improves cellular maintenance and hepatic function. *Nat. Med.* **14**, 959–965 (2008).
31. Reynolds, C. A. et al. Restoration of LAMP2A expression in old mice leads to changes in the T cell compartment that support improved immune function. *Proc. Natl Acad. Sci. USA* **121**, e2322929121 (2024).
32. Dong, S. et al. Monitoring spatiotemporal changes in chaperone-mediated autophagy in vivo. *Nat. Commun.* **11**, 645 (2020).
33. Lemaitre, J. F. et al. Sex differences in adult lifespan and aging rates of mortality across wild mammals. *Proc. Natl Acad. Sci. USA* **117**, 8546–8553 (2020).
34. Xirocostas, Z. A., Everingham, S. E. & Moles, A. T. The sex with the reduced sex chromosome dies earlier: a comparison across the tree of life. *Biol. Lett.* **16**, 20190867 (2020).
35. Tabula Muris, C. A single-cell transcriptomic atlas characterizes ageing tissues in the mouse. *Nature* **583**, 590–595 (2020).
36. Koga, H., Martinez-Vicente, M., Macian, F., Verkhusha, V. V. & Cuervo, A. M. A photoconvertible fluorescent reporter to track chaperone-mediated autophagy. *Nat. Commun.* **2**, 386 (2011).
37. Juste, Y. R. et al. Reciprocal regulation of chaperone-mediated autophagy and the circadian clock. *Nat. Cell Biol.* **23**, 1255–1270 (2021).
38. Cuervo, A. M., Dice, J. F. & Knecht, E. A population of rat liver lysosomes responsible for the selective uptake and degradation of cytosolic proteins. *J. Biol. Chem.* **272**, 5606–5615 (1997).
39. Kluever, V. et al. Protein lifetimes in aged brains reveal a proteostatic adaptation linking physiological aging to neurodegeneration. *Sci. Adv.* **8**, eabn4437 (2022).
40. Arleo, A. et al. Consensus paper: cerebellum and ageing. *Cerebellum* **23**, 802–832 (2023).
41. Rodriguez-Muela, N. et al. Balance between autophagic pathways preserves retinal homeostasis. *Aging Cell* **12**, 478–488 (2013).
42. Kaushik, S. & Cuervo, A. M. Degradation of lipid droplet-associated proteins by chaperone-mediated autophagy facilitates lipolysis. *Nat. Cell Biol.* **17**, 759–770 (2015).
43. Selman, M. & Pardo, A. Fibroageing: an ageing pathological feature driven by dysregulated extracellular matrix-cell mechanobiology. *Ageing Res. Rev.* **70**, 101393 (2021).
44. Tukiainen, T. et al. Landscape of X chromosome inactivation across human tissues. *Nature* **550**, 244–248 (2017).
45. Dror, I., Tan, T. & Plath, K. A critical role for X-chromosome architecture in mammalian X-chromosome dosage compensation. *Curr. Opin. Genet. Dev.* **87**, 102235 (2024).
46. Kanno, H., Handa, K., Murakami, T., Aizawa, T. & Ozawa, H. Chaperone-mediated autophagy in neurodegenerative diseases and acute neurological insults in the central nervous system. *Cells* **11**, 1205 (2022).
47. Kallergi, E. & Nikoletopoulou, V. Macroautophagy and normal aging of the nervous system: lessons from animal models. *Cell Stress* **5**, 146–166 (2021).
48. Gamerdinger, M. et al. Protein quality control during aging involves recruitment of the macroautophagy pathway by BAG3. *EMBO J.* **28**, 889–901 (2009).
49. Small, S. A., Chawla, M. K., Buonocore, M., Rapp, P. R. & Barnes, C. A. Imaging correlates of brain function in monkeys and rats isolates a hippocampal subregion differentially vulnerable to aging. *Proc. Natl Acad. Sci. USA* **101**, 7181–7186 (2004).
50. Devanand, D. P. et al. Hippocampal and entorhinal atrophy in mild cognitive impairment: prediction of Alzheimer disease. *Neurology* **68**, 828–836 (2007).
51. Juottonen, K. et al. Volumes of the entorhinal and perirhinal cortices in Alzheimer's disease. *Neurobiol. Aging* **19**, 15–22 (1998).
52. Feng, X. et al. Brain regions vulnerable and resistant to aging without Alzheimer's disease. *PLoS ONE* **15**, e0234255 (2020).
53. Caballero, B. et al. Acetylated tau inhibits chaperone-mediated autophagy and promotes tau pathology propagation in mice. *Nat. Commun.* **12**, 2238 (2021).
54. Janmaat, S. et al. Age-related Purkinje cell death is steroid dependent: RORα haplo-insufficiency impairs plasma and cerebellar steroids and Purkinje cell survival. *Age (Dordr.)* **33**, 565–578 (2011).
55. Andersen, B. B., Gundersen, H. J. & Pakkenberg, B. Aging of the human cerebellum: a stereological study. *J. Comp. Neurol.* **466**, 356–365 (2003).
56. Organisciak, D. T. & Vaughan, D. K. Retinal light damage: mechanisms and protection. *Prog. Retin. Eye Res.* **29**, 113–134 (2010).
57. Kolesnikov, A. V., Fan, J., Crouch, R. K. & Kefalov, V. J. Age-related deterioration of rod vision in mice. *J. Neurosci.* **30**, 11222–11231 (2010).
58. Sasaki, M. et al. Gender-specific association of early age-related macular degeneration with systemic and genetic factors in a Japanese population. *Sci. Rep.* **8**, 785 (2018).
59. Handa, K. et al. Chaperone-mediated autophagy after spinal cord injury. *J. Neurotrauma* **37**, 1687–1695 (2020).
60. Zhang, Z. et al. Sirt1 attenuates astrocyte activation via modulating Dnajb1 and chaperone-mediated autophagy after closed head injury. *Cereb. Cortex* **32**, 5191–5205 (2022).
61. di Domenico, A. et al. Patient-specific iPSC-derived astrocytes contribute to non-cell-autonomous neurodegeneration in Parkinson's disease. *Stem Cell Rep.* **12**, 213–229 (2019).
62. Van Hoesen, G. W., Hyman, B. T. & Damasio, A. R. Entorhinal cortex pathology in Alzheimer's disease. *Hippocampus* **1**, 1–8 (1991).
63. Hilmer, S. N., Cogger, V. C. & Le Couteur, D. G. Basal activity of Kupffer cells increases with old age. *J. Gerontol. A Biol. Sci. Med. Sci.* **62**, 973–978 (2007).
64. Stahl, E. C., Haschak, M. J., Popovic, B. & Brown, B. N. Macrophages in the aging liver and age-related liver disease. *Front. Immunol.* **9**, 2795 (2018).
65. Gukovskaya, A. S. & Gukovsky, I. Autophagy and pancreatitis. *Am. J. Physiol. Gastrointest. Liver Physiol.* **303**, G993–G1003 (2012).
66. Logsdon, C. D. & Ji, B. The role of protein synthesis and digestive enzymes in acinar cell injury. *Nat. Rev. Gastroenterol. Hepatol.* **10**, 362–370 (2013).
67. Wang, M., Gorelick, F. & Bhargava, A. Sex differences in the exocrine pancreas and associated diseases. *Cell Mol. Gastroenterol. Hepatol.* **12**, 427–441 (2021).
68. Jiménez-Loygorri, J. I. et al. Mitophagy curtails cytosolic mtDNA-dependent activation of cGAS/STING inflammation during aging. *Nat. Commun.* **15**, 830 (2024).
69. Ou, M. Y., Zhang, H., Tan, P. C., Zhou, S. B. & Li, Q. F. Adipose tissue aging: mechanisms and therapeutic implications. *Cell Death Dis.* **13**, 300 (2022).
70. Cuervo, A. M., Knecht, E., Terlecky, S. R. & Dice, J. F. Activation of a selective pathway of lysosomal proteolysis in rat liver by prolonged starvation. *Am. J. Physiol.* **269**, C1200–C1208 (1995).

71. Rosselot, C. et al. Myc is required for adaptive β-cell replication in young mice but is not sufficient in one-year-old mice fed with a high-fat diet. *Diabetes* **68**, 1934–1949 (2019).
72. Schindelin, J. et al. Fiji: an open-source platform for biological-image analysis. *Nat. Methods* **9**, 676–682 (2012).
73. Gilles, J. F., Dos Santos, M., Boudier, T., Bolte, S. & Heck, N. DiAna, an ImageJ tool for object-based 3D co-localization and distance analysis. *Methods* **115**, 55–64 (2017).
74. Van Rossum, G. & Drake, F. L. *Python 3 Reference Manual (Python Documentation Manual Part 2)* (CreateSpace, 2009).
75. Farewell, V. T., Long, D. L., Tom, B. D. M., Yiu, S. & Su, L. Two-part and related regression models for longitudinal data. *Annu. Rev. Stat. Appl.* **4**, 283–315 (2017).
76. Lachenbruch, P. A. Comparisons of two-part models with competitors. *Stat. Med.* **20**, 1215–1234 (2001).

Acknowledgements

We thank the Histology and Comparative Pathology core facilities at Albert Einstein College of Medicine. This work was supported by grants from the National Institutes of Health (NIH) (AG021904, AG054108 and DK098408 (to A.M.C.) and AG031782 (to A.M.C. and M.K.)), the generous support of the Hevolution Foundation, JPB Foundation, the Rainwaters Foundation, Robert and Renee Belfer (to A.M.C.) and the Grace Science Foundation (to S.K.). R.R.K. was supported by an IRACDA-BETTR grant and NIH T32AGAG023475, A.M.-S. by a Ramon Areces Postdoctoral Fellowship, A.M.-G. by a Margarita Salas contract for young PhD training, R.G.-S. by PID2021-126864NB I00 from MCIN (Spain), E.A. by NIH DK124308, M.M. by NIH T32AG023475, M.J. by NIH T32HL14445 and R.S. by NIH T32GM007491 and NIH F31 AG084192.

Author contributions

R.R.K. performed experiments and analyzed CMA in neuronal cells in brain regions, coordinated image-based and biochemical experiments, integrated data and figures across the tissues and prepared the first paper draft and the revised version. A.M.-S. performed calculations of CMA, macroautophagy and lysosomal transcriptional index, analysis of hormone receptors and *Xist* expression for all tissues, computational integration of CMA activity data across tissues and organs and contributed to and edited the paper. X.X. and M.K. performed and reviewed all the statistical analyses and edited the paper. The following authors performed experiments and analyzed CMA in the indicated tissues and read and edited the paper: O.S.-F. (kidney, skeletal muscle and pancreas), R.S. and M.M. (cardiomyocytes), A.M.-G. (pancreas cells), M.J. (liver cells), A.S. (astrocytes in brain regions) and R.G.-S. (photoreceptors in retina). K.L. assisted with RT–qPCR, and K.L. and B.C. assisted with mouse breeding, genotype and tissue dissection. A.R.S.-I., I.T. and E.A. contributed conceptually to analysis and quantification procedures. S.K. performed experiments and analyzed CMA in adipose tissues, performed biochemical analysis and helped with training of quantification procedures and editing of the first draft and of the final paper. A.M.C. conceived and directed the study, contributed to paper writing and edited the final version of the paper.

Competing interests

A.M.C. is a co-founder and scientific advisor for the autophagy program at Life Biosciences. The other authors declare no competing interests relating to this work.

Additional information

Extended data is available for this paper at https://doi.org/10.1038/s43587-024-00799-6.

Supplementary information The online version contains supplementary material available at https://doi.org/10.1038/s43587-024-00799-6.

Correspondence and requests for materials should be addressed to Rabia R. Khawaja or Ana Maria Cuervo.

Peer review information *Nature Aging* thanks Evandro Fang, Yuya Nishida and the other, anonymous, reviewer(s) for their contribution to the peer review of this work.

Reprints and permissions information is available at www.nature.com/reprints.

Publisher's note Springer Nature remains neutral with regard to jurisdictional claims in published maps and institutional affiliations.

[1]Department of Developmental and Molecular Biology, Albert Einstein College of Medicine, Bronx, NY, USA. [2]Institute for Aging Research, Albert Einstein College of Medicine, Bronx, NY, USA. [3]Department of Biochemistry, Albert Einstein College of Medicine, Bronx, NY, USA. [4]Department of Biochemistry and Molecular Biology, University of Córdoba, Córdoba, Spain. [5]Department of Medicine, Marion Bessin Liver Research Center, Albert Einstein College of Medicine, Bronx, NY, USA. [6]Department of Epidemiology and Population Health, Albert Einstein College of Medicine, Bronx, NY, USA. [7]Present address: IMDEA Food, Madrid, Spain. [8]Present address: Bellvitge Biomedical Research Institute, IDIBELL, University of Barcelona, Barcelona, Spain. [9]Present address: Department of Cellular and Molecular Biology, Centro de Investigaciones Biológicas Margarita Salas, CSIC, Madrid, Spain. [10]These authors contributed equally: Rabia R. Khawaja, Adrián Martín-Segura. ✉e-mail: rabia.khawaja@einsteinmed.edu; ana-maria.cuervo@einsteinmed.edu

https://doi.org/10.1038/s43587-024-00799-6

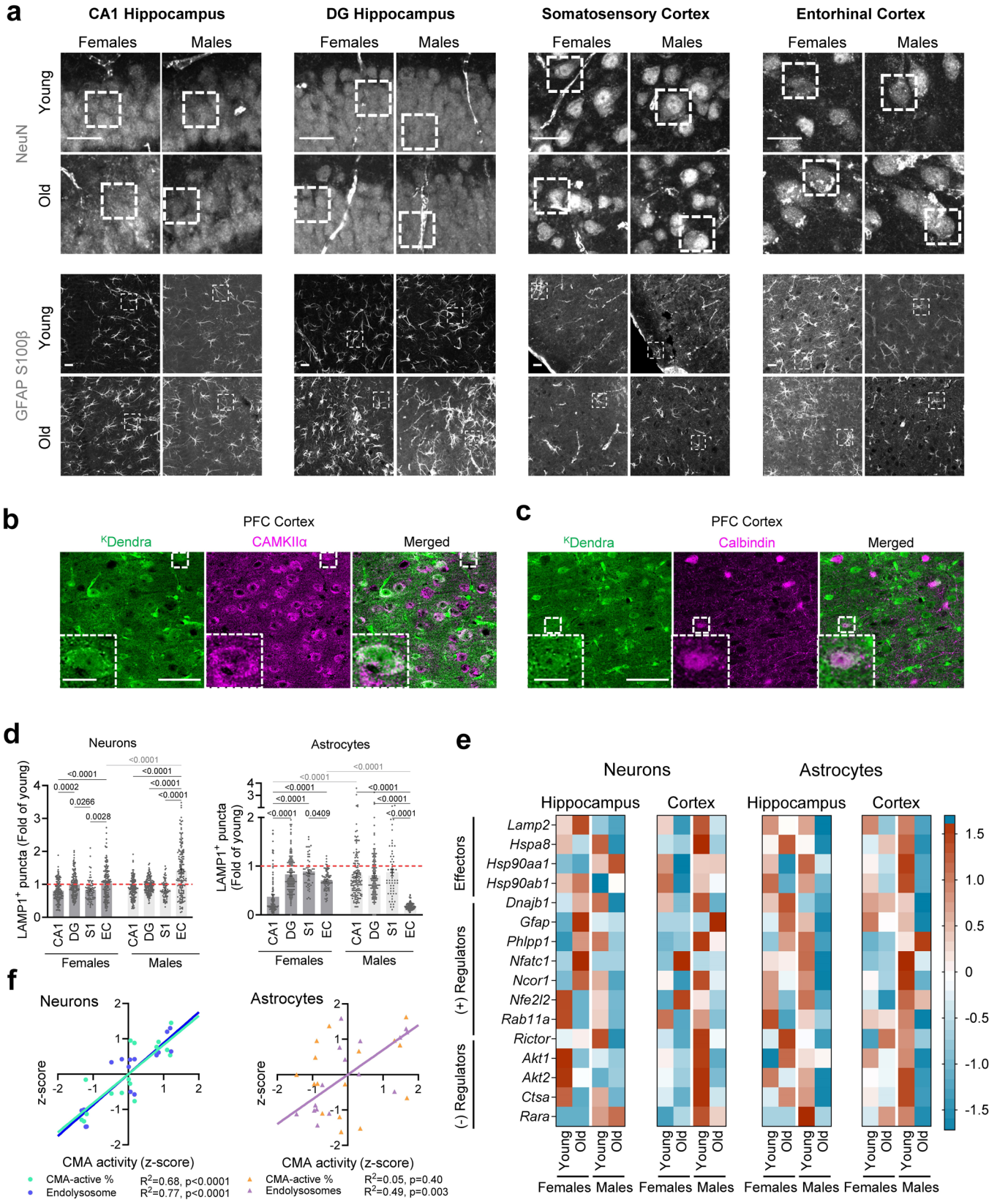

Extended Data Fig. 1 | See next page for caption.

https://doi.org/10.1038/s43587-024-00799-6

Extended Data Fig. 1 | Region-specific changes with age in neuronal and astrocytic CMA. a, Confocal images of the indicated brain regions from young (4-6 m) and old (24-28 m) female and male ^{KFERQ}Dendra mice stained for the neuronal marker NeuN$^+$ (top) or the astrocyte markers GFAP$^+$S100β$^+$ (bottom). Scale bars, 25μm (top), 20μm (bottom). Boxed areas indicate the regions displayed at higher magnification in main Fig. 1 (**a,e,i,m**) and 2 (**a,e,i,m**). **b,c**, Confocal images of prefrontal cortex (PFC) regions stained for ^{K}Dendra and the excitatory neuron marker CAMKIIα (**b**) or the inhibitory neuronal markers Calbindin (**c**). Insets: Higher magnification of neurons in the boxed areas. Scale bars, 5μm (left), 25μm (right). **d**, Quantification of changes in LAMP1$^+$ puncta in neurons (left) and astrocytes (right) from the indicated brain regions of old male and female mice relative to those in sex-matched young mice. Values are mean ± s.e.m. Number mice(cells) for YF, OF, YM and OM, respectively are indicated in legends of main Figs. 1 and 2 and summarized in Source data Extended Data Fig. 1. **e**, Normalized expression (z scoring within each cell type and brain region) of the CMA network components (organized in functional groups) in excitatory neurons and astrocytes in hippocampal and cortical region from young (3 m) and old (18-24 m) male and female mice, calculated from single cell RNAseq data from the Tabula Muris Senis dataset. **f**, Correlation analysis of CMA activity (^{K}Dendra$^+$LAMP1$^+$ z-score) against endolysosome abundance (LAMP1$^+$ puncta z-score) or percentage of CMA competent lysosomes (^{K}Dendra$^+$LAMP1$^+$ [% of LAMP1$^+$] z-score) in neurons (left) and astrocytes (right) in brains of the young and old, females and males mice used in Figs. 1 and 2. *P* values were calculated using two-way ANOVA with Bonferroni's multiple comparison test (**d**) or simple linear regression (**e**). All values were compared, but only significant comparisons are marked. A linear regression line is plotted on graphs with significant correlations with either an R^2 value between 0.1-0.5 (when P-value < 0.05) or an R^2 value > 0.5.

https://doi.org/10.1038/s43587-024-00799-6

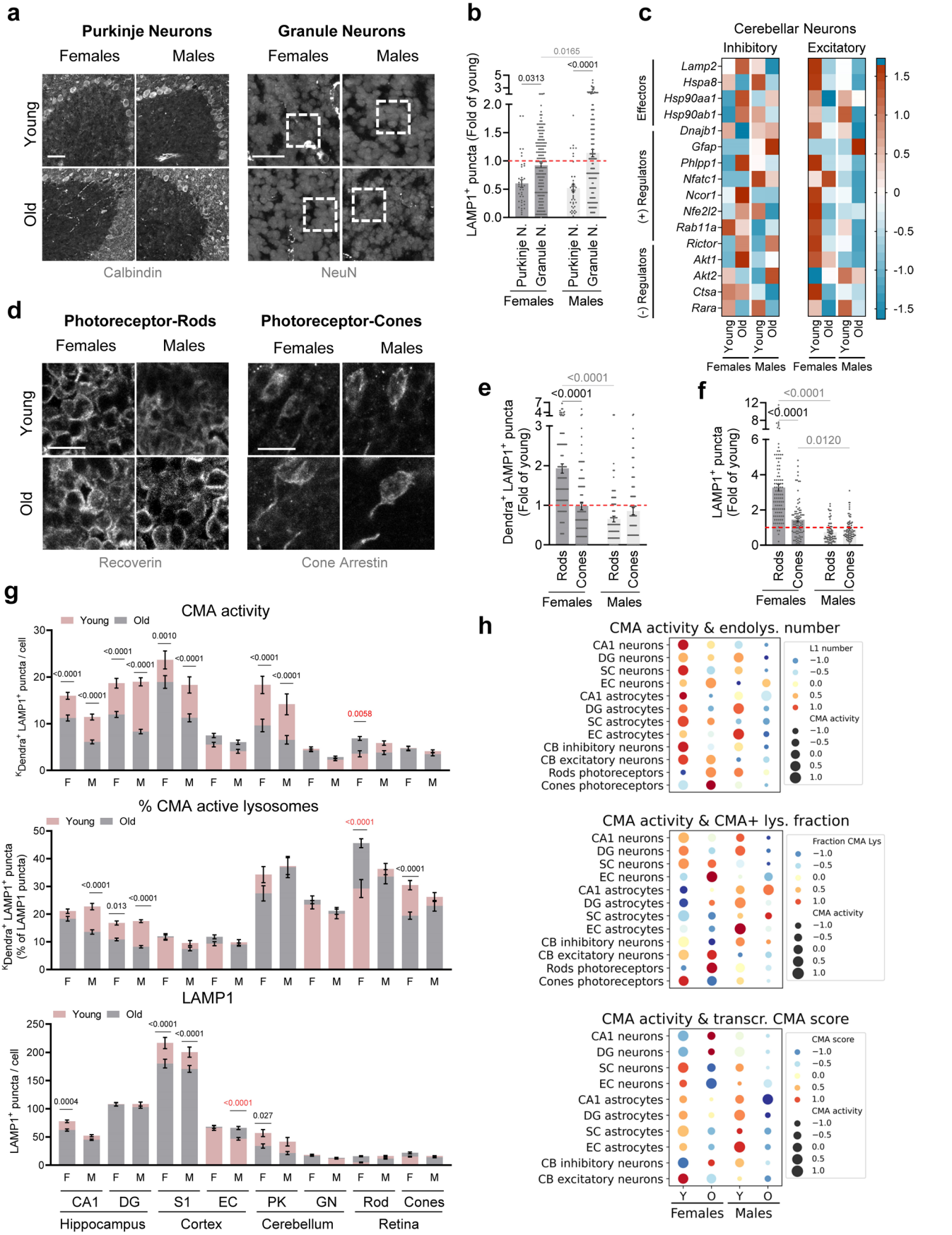

Extended Data Fig. 2 | See next page for caption.

https://doi.org/10.1038/s43587-024-00799-6

Extended Data Fig. 2 | Sex and cell type-specific changes in brain and retina with age. a, Confocal images of cerebellum from young (4-6 m) and old (24-28 m) female and male ^{KFERQ}Dendra mice stained with Calbindin^{+} (left) or NeuN^{+} (right) to highlight Purkinje and Granule neurons, respectively. Boxed areas are displayed at higher magnification in main Fig. 3 **a**,**e**. Scale bars, 50µm (left), 25µm (right). **b**, Changes in LAMP1^{+} puncta in Purkinje and Granule neurons of old mice relative to sex-matched young mice. **c**, Normalized expression (z scoring) of the CMA network components in excitatory and inhibitory cerebellar neurons from young (3 m) and old (18-24 m) male and female mice, calculated from single cell RNAseq data from the Tabula Muris Senis dataset. **d**, Confocal images of retina from same mice as in **a** stained with Recoverin (left) or Arrestin (right) to highlight rods and cones in retina. Scale bars, 10µm. **e, f**, Number of ^{K}Dendra^{+} and LAMP1^{+} puncta (**e**) and LAMP1^{+} puncta (**f**) in retinal cells from old mice relative to sex-matched young mice. **g**, CMA activity (^{K}Dendra^{+}LAMP1^{+} puncta, top), percentage of CMA-active LAMP1^{+} lysosomes (middle), and endolysosome content (LAMP1^{+}puncta, bottom) across the neuronal subtypes analyzed in young and old, female (F) and male (M) mice. **h**, Bubble plots of changes in CMA activity z-score (^{K}Dendra^{+}LAMP1^{+} puncta, balloon size) compared with endolysosome number (top), fraction of CMA-active lysosomes (middle), and CMA transcriptional z-score (bottom) in the indicated neuronal types and astrocytes from brain regions from young (Y) and old (O) male and female mice. Data presented as mean ± s.e.m. Number mice(cells) for YF, OF, YM and OM, respectively are indicated in legends of main Fig. 3 (for **b, e** and **f**) and 1 and 3 (for **g**) and summarized in Source data Extended Data Fig. 2. *P* values were calculated using two-way ANOVA with Bonferroni's multiple comparison test. All values were compared, but only significant comparisons are marked.

https://doi.org/10.1038/s43587-024-00799-6

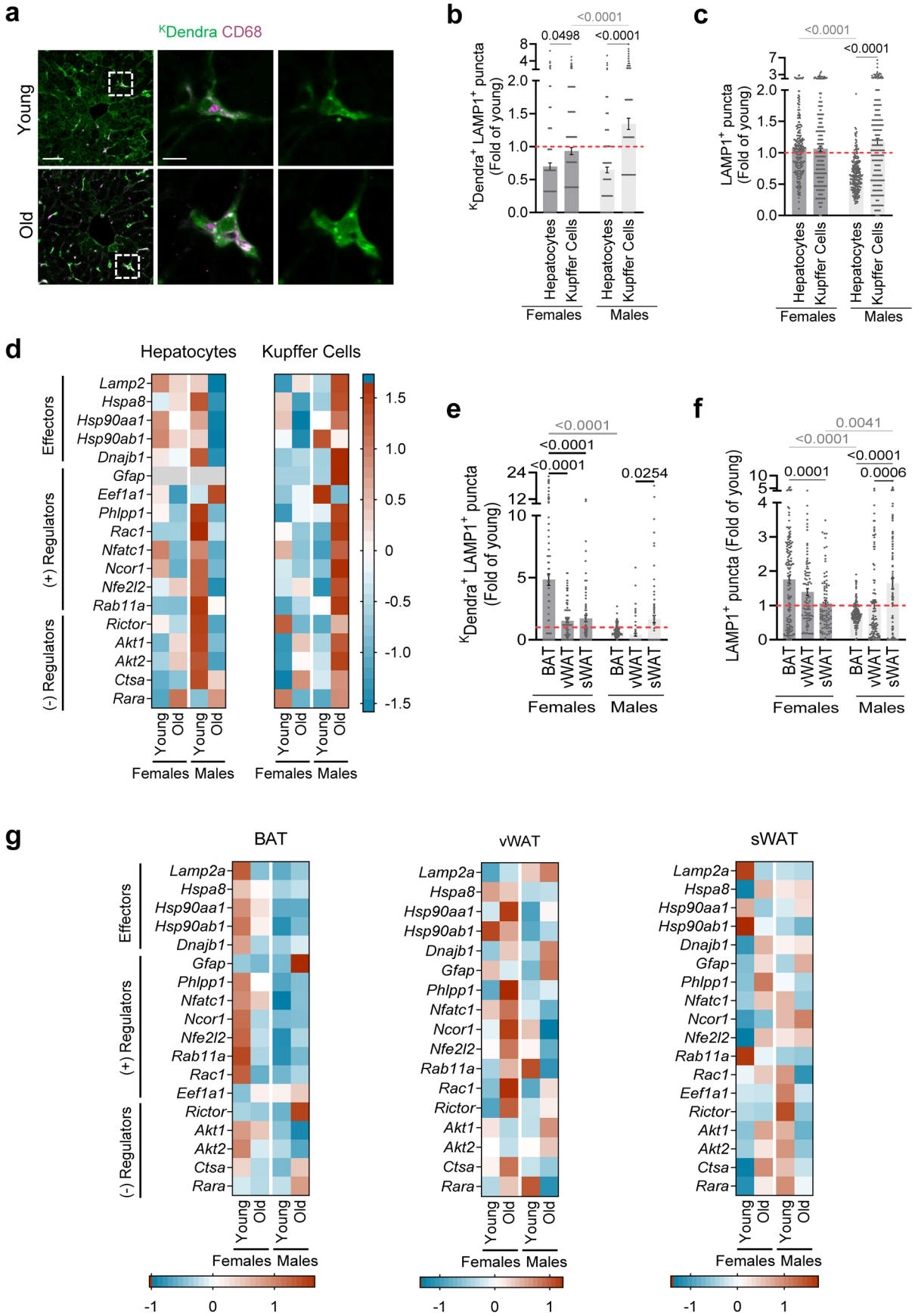

Extended Data Fig. 3 | See next page for caption.

https://doi.org/10.1038/s43587-024-00799-6

Extended Data Fig. 3 | Changes with age in the CMA transcriptional network in peripheral tissues. a, Confocal images of livers from male young (4-6 m) and old (24-28 m) ^{KFERQ}Dendra mice stained for ^{K}Dendra and CD68 to highlight Kupffer cells. Middle and right panels: higher magnification of boxed region in left. Scale bars, 50μm (left), 10μm (right). **b,c**, and **e,f**. Quantification of changes in ^{K}Dendra^{+}LAMP1^{+} puncta (**b,e**) and in LAMP1^{+} puncta levels (**c,f**) in liver cells (**b,c**) and adipose tissues (**e,f**) of old male and female mice relative to those in sex-matched young mice. **d**,**g**. Normalized expression (z scoring within each cell type and tissue) of the CMA network components (organized in functional groups) in liver (**d**) and adipose tissues (**g**) from young (3 m) and old (18-24 m) male and female mice, calculated from single cell RNAseq data from the Tabula Muris Senis dataset. Values are mean ± s.e.m. and individual values. Number mice(cells) for YF, OF, YM and OM, respectively are indicated in legends of main Fig. 4 (for **b, c**) and 5 (for **e** and **f**) and summarized in Source data Extended Data Fig. 3. *P* values were calculated using two-way ANOVA with Bonferroni's multiple comparison test. All values were compared, but only significant comparisons are marked.

https://doi.org/10.1038/s43587-024-00799-6

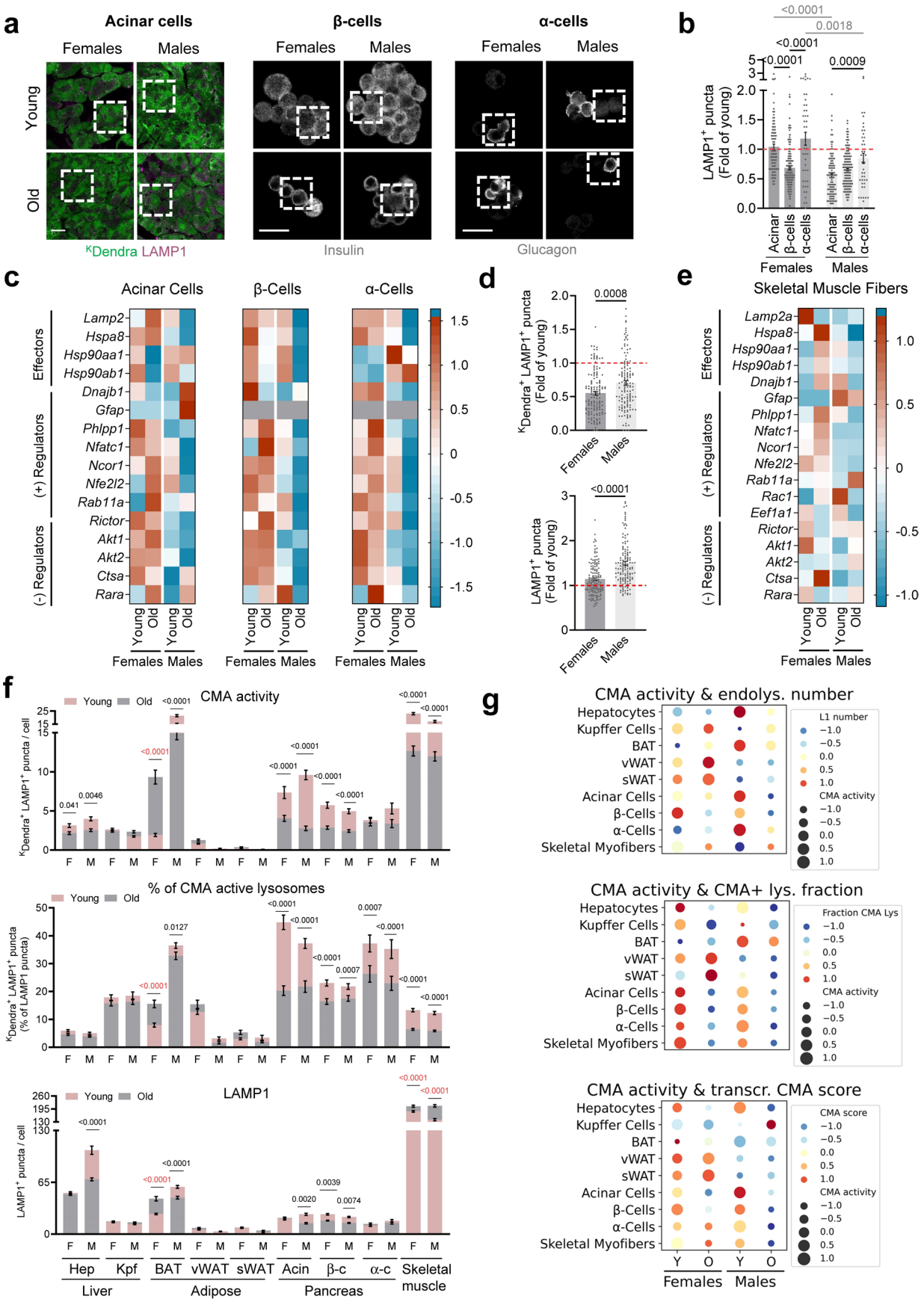

Extended Data Fig. 4 | See next page for caption.

https://doi.org/10.1038/s43587-024-00799-6

Extended Data Fig. 4 | Decline of CMA in aging pancreas and skeletal muscles. **a**, Confocal images of pancreas (left) and isolated Islets of Langerhans (middle and right) from young (4-6 m) and old (24-28 m) female and male ^{KFERQ}Dendra mice stained with ^{K}Dendra and LAMP1 (exocrine pancreas, left), insulin (β-cells, middle) and glucagon (α-cells, right). Boxed areas are displayed at higher magnification in main Fig. 5 **a,e,i**. Scale bars, 30μm (left) and 20μm (middle and right). **b,d**. Number of LAMP1^{+} puncta in pancreas and of ^{K}Dendra^{+}LAMP1^{+} puncta (top) and LAMP1^{+} (bottom) in skeletal muscle fibers from of old mice relative to those in sex-matched young mice. **c,e**, Normalized expression (z scoring) of the CMA network components in pancreas (**c**) and skeletal muscle (**e**) from young (3 m) and old (18-24 m) male and female mice, calculated from single cell RNAseq data from the Tabula Muris Senis dataset. **f**, CMA activity (^{K}Dendra^{+}LAMP1^{+} puncta, top), percentage of CMA-active LAMP1^{+} lysosomes (middle), and endolysosomes (LAMP1^{+}puncta, bottom) compared across all the analyzed cells in liver, adipose tissues, pancreas and skeletal muscles in young and old, female (F) and male (M) mice. Values are mean ± s.e.m. and n values those indicated in main Figs. 4 and 5. **g**, Bubble plots to illustrate changes in CMA activity z-score (^{K}Dendra^{+}LAMP1^{+} puncta, ballon size) compared with number of endolysosomes z-score (top), fraction of CMA-active lysosomes z-score, (middle), and CMA transcriptional z-score (bottom) in liver, adipose tissue, pancreas and skeletal muscle cells from young (Y) and old (O) female and male mice. Data presented as mean ± s.e.m. and individual data (for **b** and **d**). Number mice(cells) for YF, OF, YM and OM, respectively are indicated in legends of main Fig. 5 (for **b, c**) and 4 and 5 (for **f**) and summarized in Source data Extended Data Fig. 4. *P* values were calculated using two-way ANOVA with Bonferroni's multiple comparison test (**b**) or two-tailed unpaired Student's t test (**d**) or two-way ANOVA with Fishers LSD test (**f**). All values were compared, but only significant comparisons are marked.

https://doi.org/10.1038/s43587-024-00799-6

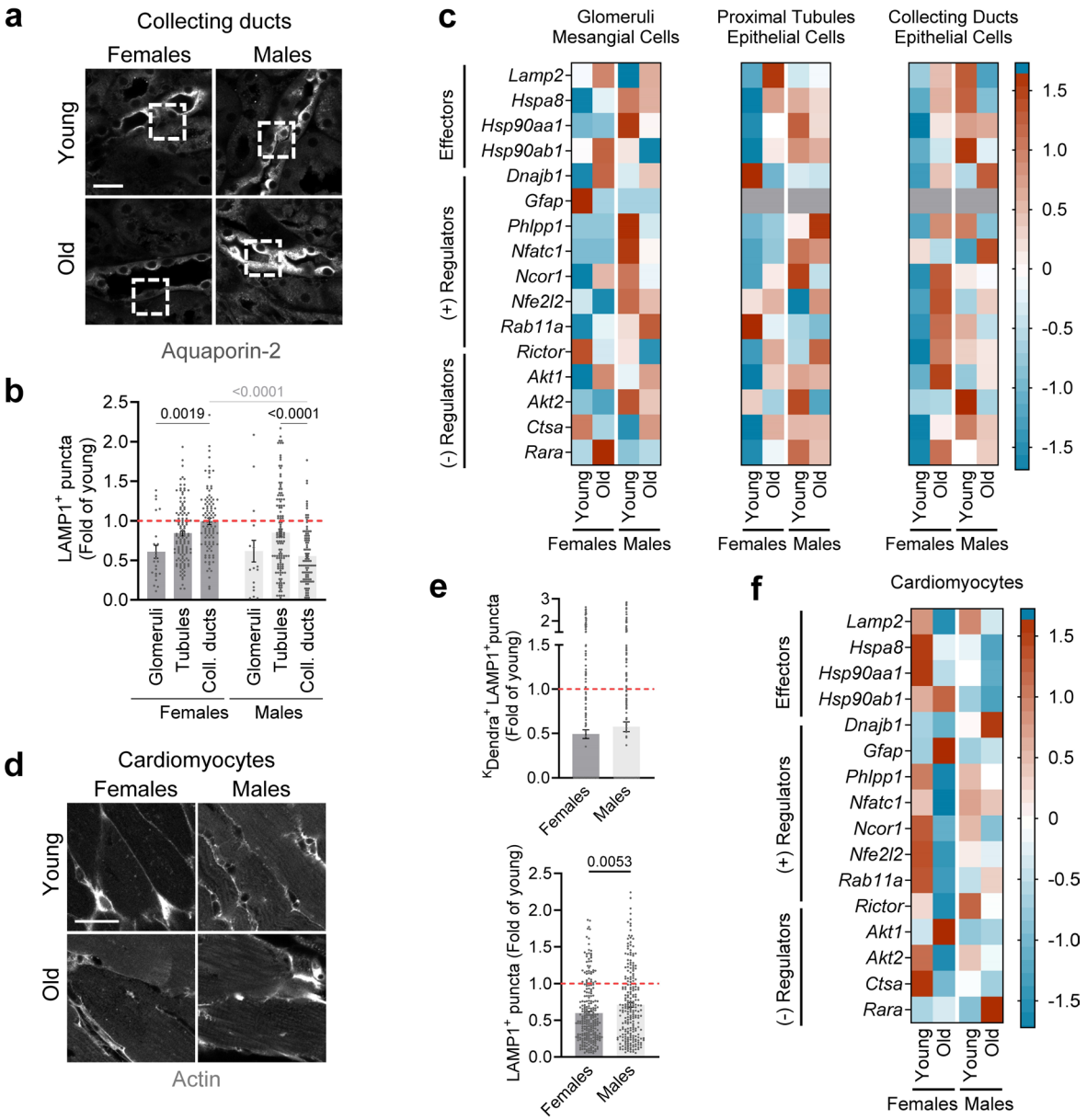

Extended Data Fig. 5 | Cell-specific changes with age in kidney and heart CMA. **a, d**, Confocal images of kidney (**a**) and heart (**d**) from female and male young (4-6 m) and old (24-28 m) ^{KFERQ}Dendra mice stained for Aquaporin-2^{+} (**a**) to stain collecting ducts and actin (**d**) for cardiomyocytes. Scale bar, 20μm (**a**). Scale bar, 10μm (**d**). Boxed areas indicate the regions displayed at higher magnification in main Fig. 6 **i. b, e**, Quantification of changes in LAMP1^{+} puncta in kidney cells (**b**) and of changes in ^{K}Dendra^{+}LAMP1^{+} puncta (top) and LAMP1^{+} (bottom) in cardiomyocytes (**e**) from of old male and female mice relative to those in sex-matched young mice. **c, f**, Normalized expression (z scoring within each cell type) of the CMA network components (organized in functional groups) in kidney (**c**) and cardiomyocytes (**f**) from young (3 m) and old (18-24 m) male and female mice, calculated from single cell RNAseq data from the Tabula Muris Senis dataset. Data presented as mean ± s.e.m. Values are mean ± s.e.m. and individual values. Number mice(cells) for YF, OF, YM and OM, respectively are indicated in legends of main Fig. 6 and summarized in Source data Extended Data Fig. 5. *P* values were calculated using two-way ANOVA with Bonferroni's multiple comparison test (**b**) or two-tailed unpaired Student's t test (**e**). All values were compared, but only significant comparisons are marked.

https://doi.org/10.1038/s43587-024-00799-6

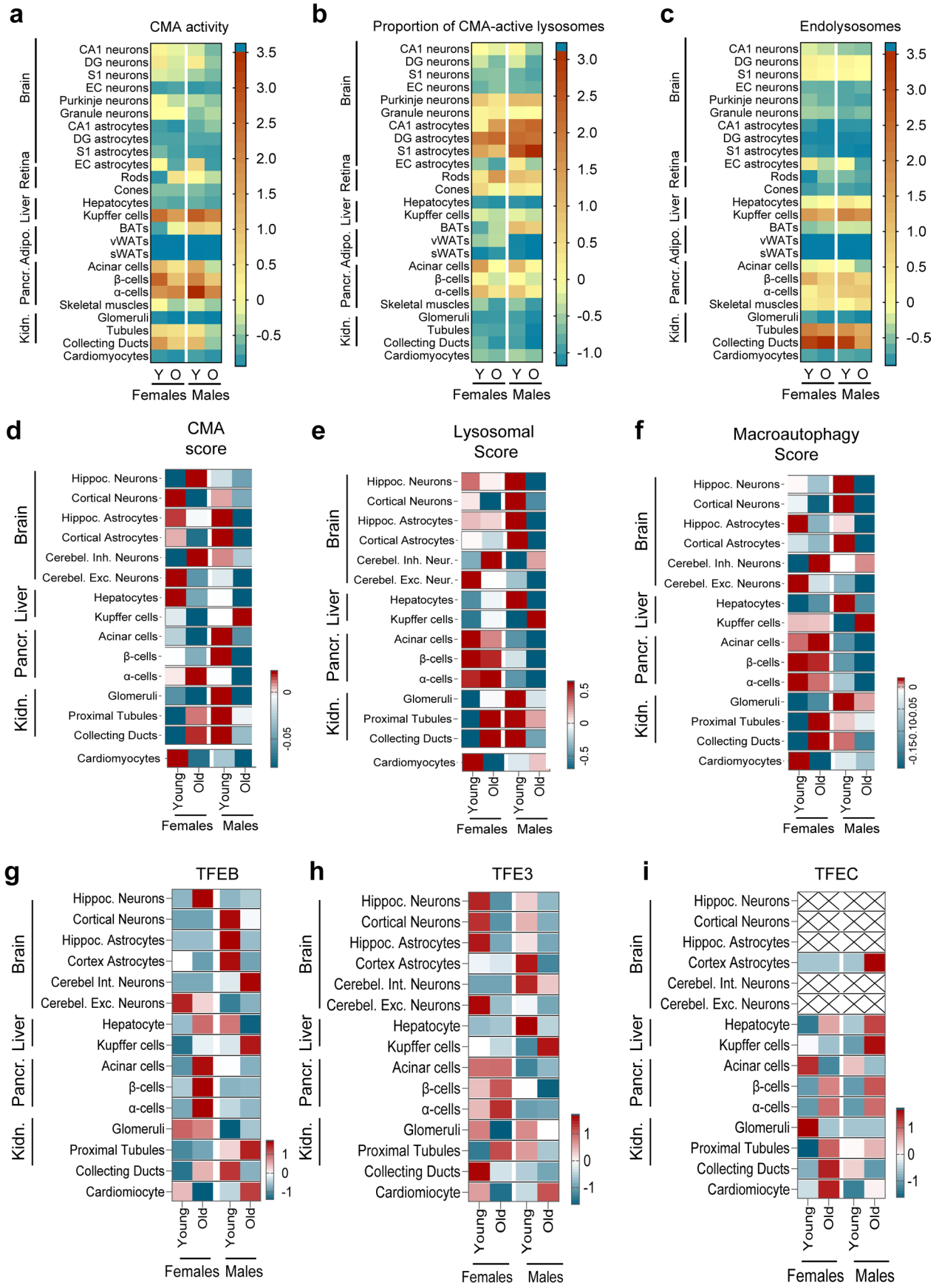

Extended Data Fig. 6 | See next page for caption.

https://doi.org/10.1038/s43587-024-00799-6

Extended Data Fig. 6 | Tissue-wide comparison of changes with age and sex in CMA and endolysosomes and in autophagy-related transcriptional programs. **a-c**, Heatmaps showing z-scores of ^{K}Dendra^{+}LAMP1^{+} puncta (CMA activity) (**a**), proportion of CMA-active lysosomes (^{K}Dendra^{+}LAMP1^{+}/LAMP1^{+}) (**b**) and LAMP1^{+} puncta (endolysosomal number) (**c**), corrected for differences in cell area (all values calculated as puncta per mm^{2} of cell area) z-scores in the indicated tissues and cell types from young (Y) and old (O) ^{KFERQ}Dendra mice. **d-f**, Transcriptional scores for CMA (**d**), endolysosomes (**e**) and macroautophagy (**f**) calculated from the individual expression of each pathway related genes in the indicated tissues and cell types from young and old female and male mice. **g-I**, Heatmaps showing normalized expression (z scoring within each cell type) of the MiTF family of transcription factors including *Tfeb* (**g**), *Tfe3* (**h**) and *Tfec* (**i**) in the indicated tissues and cell types from young and old female and male mice. Data in **d-i** was extracted from single cell RNAseq data from the Tabula Muris Senis dataset. Cell types with no data for *Tfec* in the dataset are represented with a cross.

https://doi.org/10.1038/s43587-024-00799-6

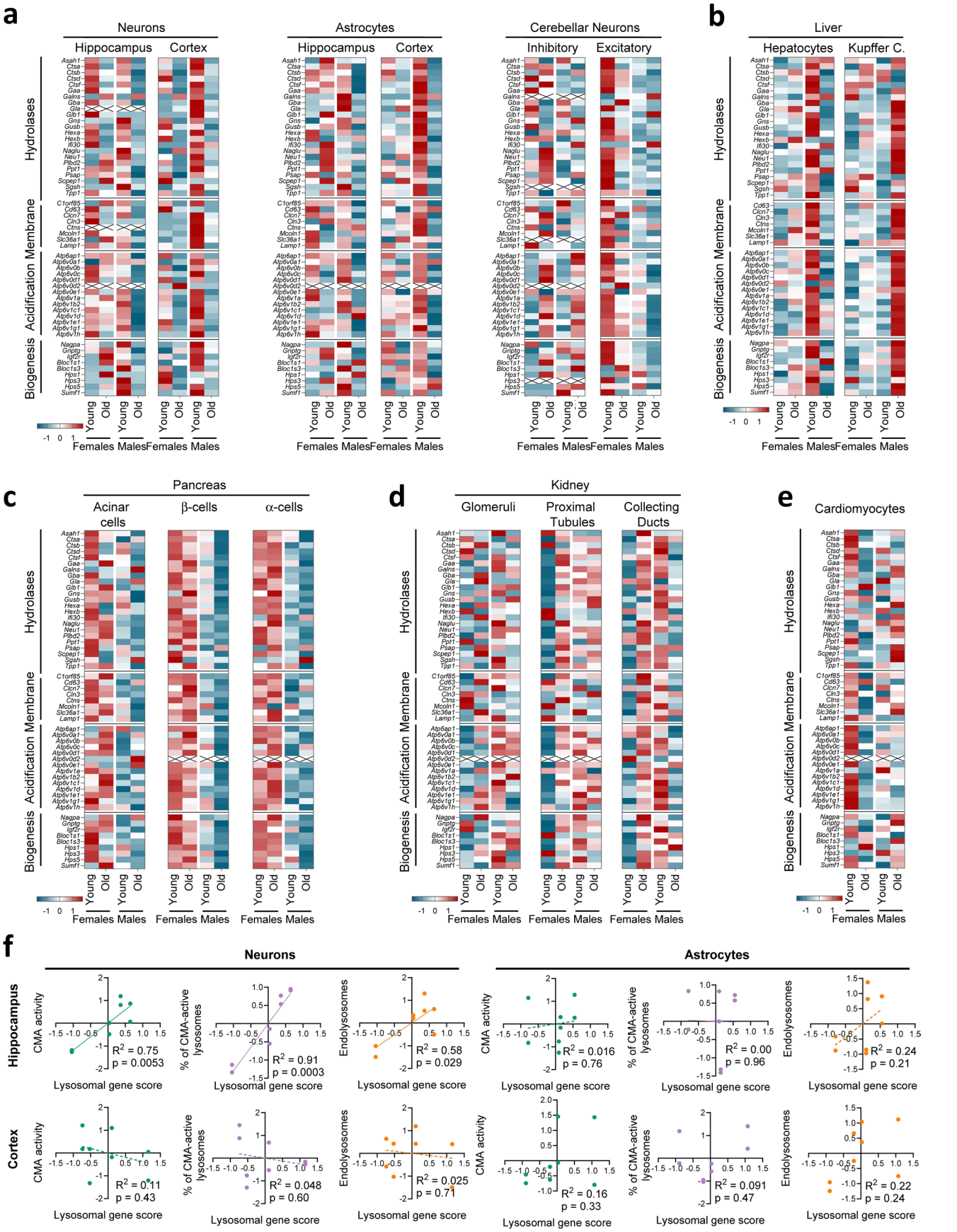

Extended Data Fig. 7 | See next page for caption.

https://doi.org/10.1038/s43587-024-00799-6

Extended Data Fig. 7 | Sex and cell-type-specific changes in expression of lysosomal genes with aging. a-e, Heatmaps showing normalized expression (z scoring within each gene) of the lysosomal components (organized in groups of lysosomal hydrolases, lysosomal membrane proteins, acidification components and biogenesis proteins) in cells of brain (**a**), liver (**b**), pancreas (**c**), kidney (**d**) and heart (**e**) from young (3 m) and old (18-24 m) female and male mice, calculated from single cell RNAseq data from the Tabula Muris Senis dataset. **f**, Correlation analysis of CMA activity (^{K}Dendra^{+}LAMP1^{+} z-score) against lysosomal gene score (averaged z-score of all lysosomal genes) in neurons (left) and astrocytes (right) of hippocampus (top) and cortex (bottom) brain regions from young and old, female and male mice used in Figs. 1 and 2. *P* values were calculated using simple linear regression. A linear regression line is plotted on graphs with significant correlations with either an R^2 value between 0.1-0.5 (when P-value < 0.05) or an R^2 value > 0.5. Cell types with no data for a certain gene in the dataset are represented with a cross.

https://doi.org/10.1038/s43587-024-00799-6

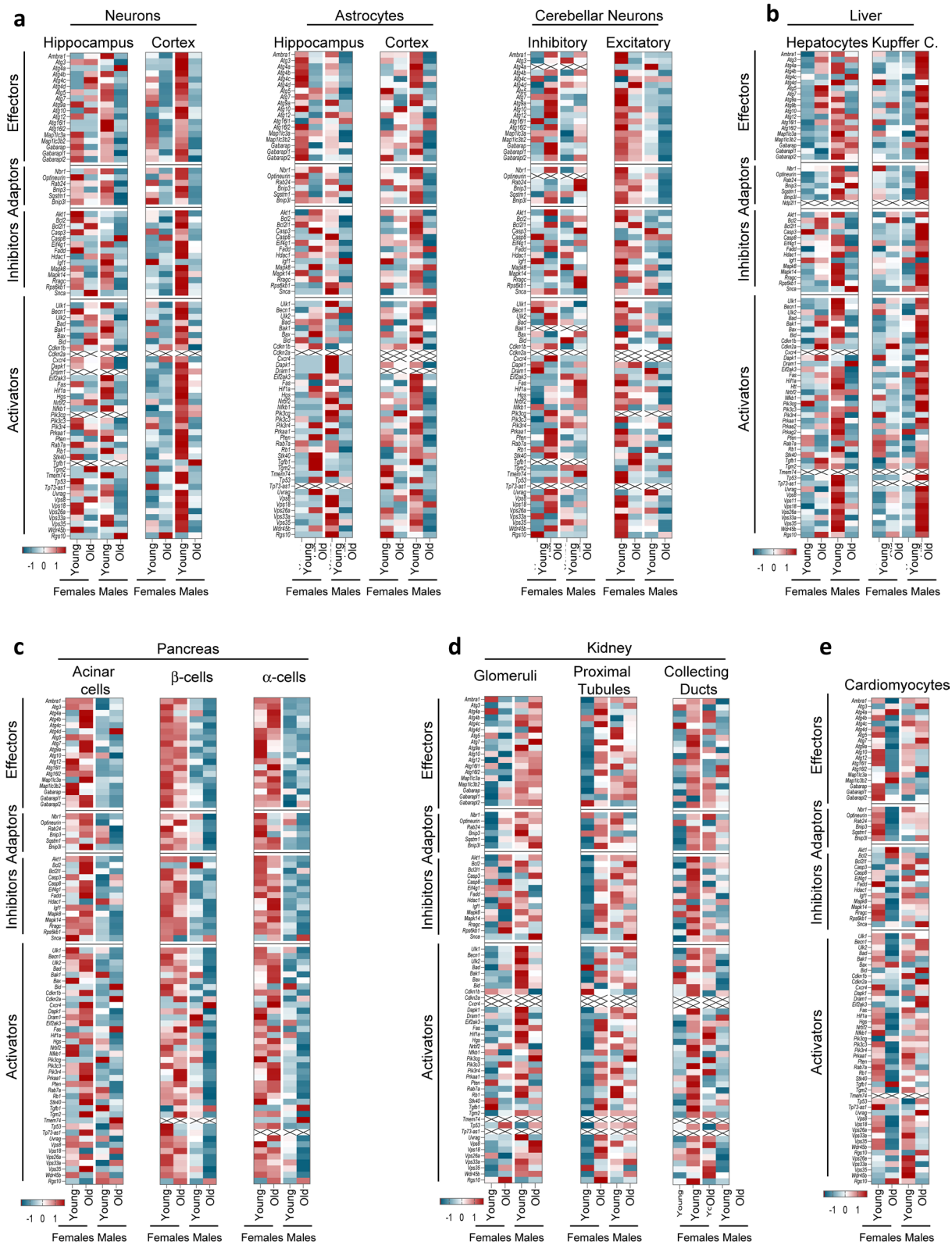

Extended Data Fig. 8 | Sex and cell-type-specific changes in expression of macroautophagy genes with aging. a-e, Heatmaps showing normalized expression (z scoring within each gene) of the macroautophagy network components (organized in functional groups of effectors, adaptors, inhibitors and activators) in cells of brain (**a**), liver (**b**), pancreas (**c**), kidney (**d**) and heart (**e**) from young (3 m) and old (18-24 m) female and male mice, calculated from single cell RNAseq data from the Tabula Muris Senis dataset. Cell types with no data for a certain gene in the dataset are represented with a cross.

https://doi.org/10.1038/s43587-024-00799-6

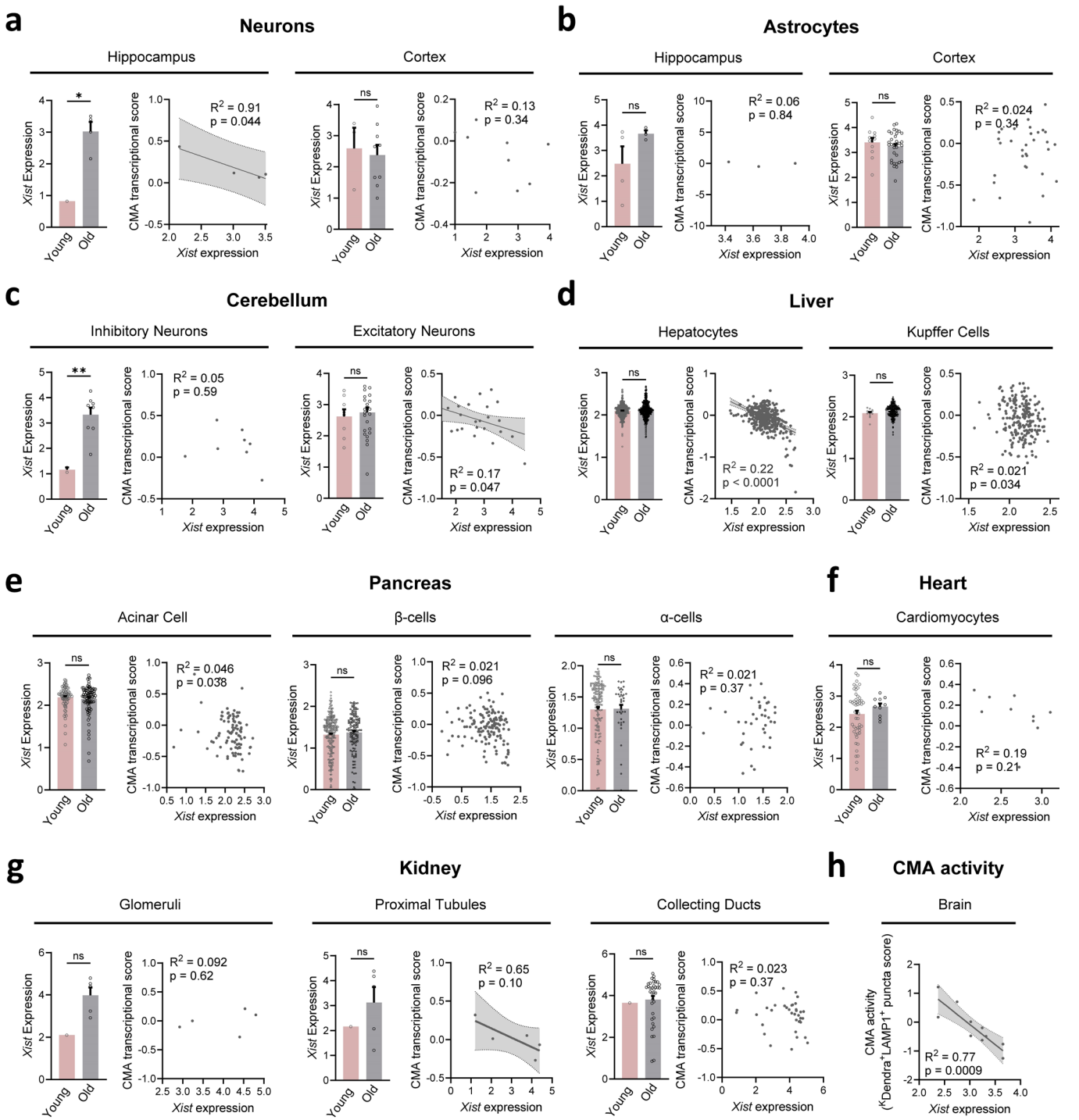

Extended Data Fig. 9 | Cell-type-specific association of CMA activity with *Xist* expression in females with aging. a-g, *Xist* expression (left panels) in young (3 m) vs old (18-24 m) female mice (when available in TMS dataset) and correlation analysis (right panels) of CMA transcriptional score against *Xist* expression in old female in the indicated cells in brain (**a-c**), liver (**d**), pancreas (**e**), heart (**f**) and kidney (**g**), calculated from single cell RNAseq data from the Tabula Muris Senis dataset. **h**, Correlation analysis of CMA activity (^{K}Dendra^{+}LAMP1^{+} z-score) against *Xist* expression in all the analyzed cell types of the brain in old females. Data presented as mean ± s.e.m. Number cells for YF, OF respectively: **a:** 1,4 (hippocampus), 3, 10 (cortex); **b:** 4, 4 (hippocampus) 11, 33 (cortex); **c**: 2, 8 (Inhibitory), 8, 24 (Excitatory); **d:** 401, 371 (Hepatocytes); 11, 213 (Kupffer cells); **e:** 73, 94 (acinar cells), 265, 140 (β-cells), 39, 39 (α-cells); **f**: 51, 10; **g:** 1, 5 (glomerulus), 5, 5 (proximal tubules), 1, 37(collecting ducts). *P < 0.05, **P < 0.01, **P < 0.001 and ****P < 0.0001 (bar graphs) or exact P values (scatter plots) were calculated using two-tailed unpaired Student's t test (left panels) or simple linear regression (right panels). A linear regression line is plotted on graphs with significant correlations with either an R^2 value between 0.1-0.5 (when P-value < 0.05) or an R^2 value > 0.5. All values were compared, but only significant comparisons are marked.

https://doi.org/10.1038/s43587-024-00799-6

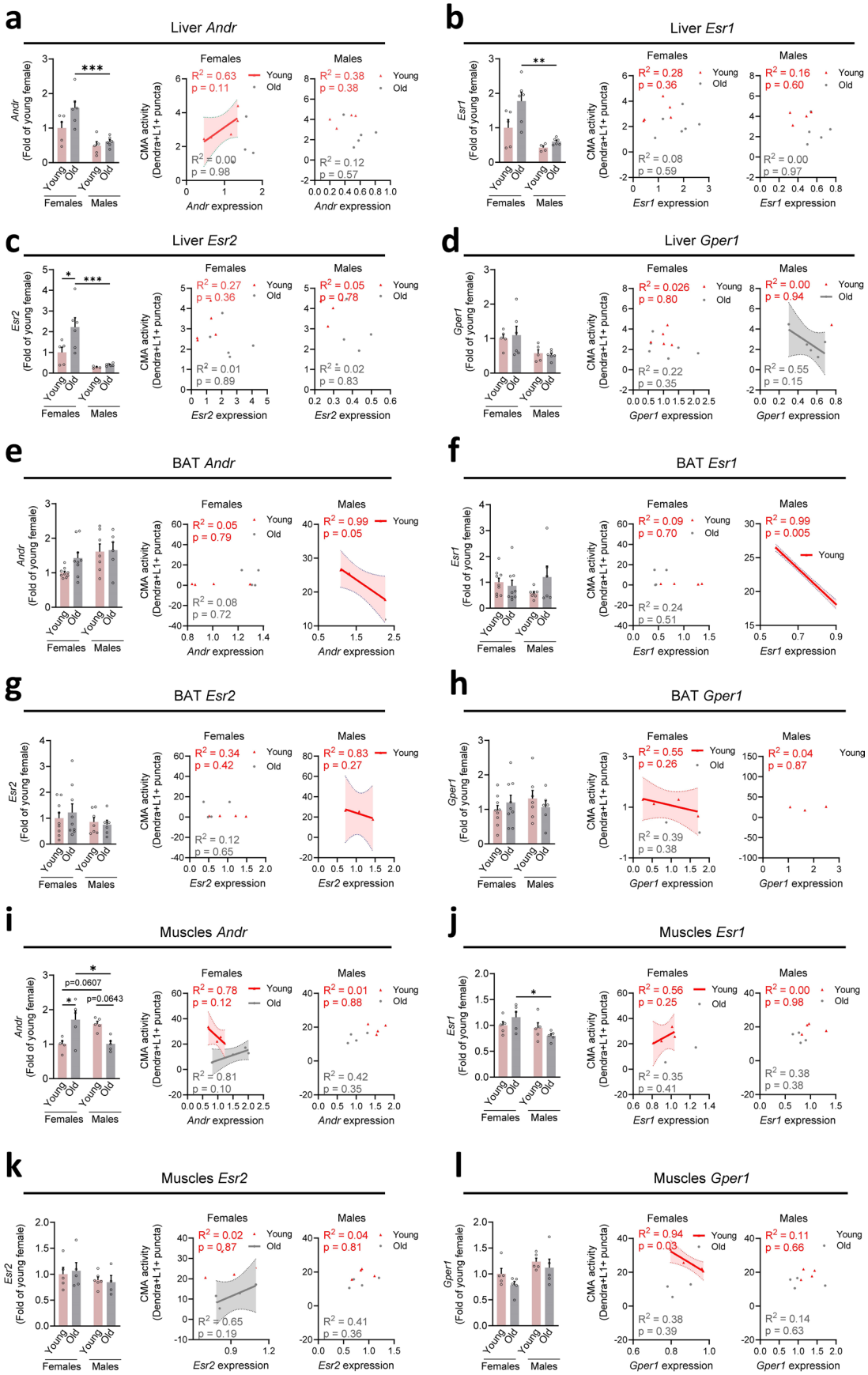

Extended Data Fig. 10 | See next page for caption.

https://doi.org/10.1038/s43587-024-00799-6

Extended Data Fig. 10 | Tissue-specific association of CMA activity with expression of sex hormone receptors in aging. a-l, Sex hormone receptors expression (left panels) and correlation analysis of their expression with CMA activity (^{K}Dendra^{+}LAMP1^{+} puncta per cell) in female (middle panels) and male (right panels) liver (**a-d**), brown adipose tissue (BAT) (**e-h**) and skeletal myofibers (**i-l**). Androgen / dihydrotestosterone receptor (*Andr*, **a,e,i**), Estrogen receptor alpha (*Esr1*, **b,f,j**), Estrogen receptor beta (*Esr2*, **c,g,k**) and G-protein coupled estrogen receptor 1 (*Gper1*, **d,h,l**) levels were measured with qRT-PCR in whole homogenate of liver, BAT and skeletal muscles in the same young (4-6 m) and old (24-28 m), female and male ^{KFERQ}Dendra mice used for CMA activity analysis (main Figs. 4 and 5). Data is presented as mean ± s.e.m. Number mice for YF, OF, YM and OM, respectively: **a-d:** 5, 6, 5, 6; **e-h:** 9, 9, 7, 6; **i-l:** 5, 5, 5, 5. *P < 0.05, **P < 0.01, **P < 0.001 and ****P < 0.0001 (bar graphs) or exact *P* values (scatter plots) were calculated using two-way ANOVA with Bonferroni's multiple comparison test (left panels) or simple linear regression (middle and right panels). A linear regression line is plotted on graphs with significant correlations with either an R^2 value between 0.1-0.5 (when P-value < 0.05) or an R^2 value > 0.5. All values were compared, but only significant comparisons are marked.

nature portfolio

Corresponding author(s): Ana Maria Cuervo
Rabia R. Khawaja

Last updated by author(s): Dec 16, 2024

Reporting Summary

Nature Portfolio wishes to improve the reproducibility of the work that we publish. This form provides structure for consistency and transparency in reporting. For further information on Nature Portfolio policies, see our Editorial Policies and the Editorial Policy Checklist.

Statistics

For all statistical analyses, confirm that the following items are present in the figure legend, table legend, main text, or Methods section.

n/a	Confirmed
☐	☒ The exact sample size (*n*) for each experimental group/condition, given as a discrete number and unit of measurement
☐	☒ A statement on whether measurements were taken from distinct samples or whether the same sample was measured repeatedly
☐	☒ The statistical test(s) used AND whether they are one- or two-sided *Only common tests should be described solely by name; describe more complex techniques in the Methods section.*
☒	☐ A description of all covariates tested
☐	☒ A description of any assumptions or corrections, such as tests of normality and adjustment for multiple comparisons
☐	☒ A full description of the statistical parameters including central tendency (e.g. means) or other basic estimates (e.g. regression coefficient) AND variation (e.g. standard deviation) or associated estimates of uncertainty (e.g. confidence intervals)
☐	☒ For null hypothesis testing, the test statistic (e.g. *F*, *t*, *r*) with confidence intervals, effect sizes, degrees of freedom and *P* value noted *Give P values as exact values whenever suitable.*
☒	☐ For Bayesian analysis, information on the choice of priors and Markov chain Monte Carlo settings
☒	☐ For hierarchical and complex designs, identification of the appropriate level for tests and full reporting of outcomes
☐	☒ Estimates of effect sizes (e.g. Cohen's *d*, Pearson's *r*), indicating how they were calculated

Our web collection on statistics for biologists contains articles on many of the points above.

Software and code

Policy information about availability of computer code

Data collection	- LAS AF Lite Leica v4.0 http://www.leicamicrosystems.com
Data analysis	- Python v3.8.16 - Fiji v1.53f and DiAna plugin NIH http://fiji.sc/ - Matplotlib v3.5.1 - Numpy v1.24.4 - Pandas v1.5.3 - Scanpy v1.9.1 - Seaborn v0.12.2. - Scikit-learn v1.0.2 - Umap-learn v0.5.3 - GraphPad Prism 9.0

For manuscripts utilizing custom algorithms or software that are central to the research but not yet described in published literature, software must be made available to editors and reviewers. We strongly encourage code deposition in a community repository (e.g. GitHub). See the Nature Portfolio guidelines for submitting code & software for further information.

Data

Policy information about availability of data

All manuscripts must include a data availability statement. This statement should provide the following information, where applicable:

- Accession codes, unique identifiers, or web links for publicly available datasets
- A description of any restrictions on data availability
- For clinical datasets or third party data, please ensure that the statement adheres to our policy

There are no restrictions on data availability in this manuscript. The single-cell RNAseq dataset used in this work is available and annotated in the repositories of the Tabula Muris Senis consortium35 (https://cellxgene.cziscience.com/collections/0b9d8a04-bb9d-44da-aa27-705bb65b54eb). All the information is included in the manuscript. All Main and Extended data Figures have associated Source Data that is provided as an Excel worksheet organized by figures, and it includes statistics along with exact p values.

Research involving human participants, their data, or biological material

Policy information about studies with human participants or human data. See also policy information about sex, gender (identity/presentation), and sexual orientation and race, ethnicity and racism.

Reporting on sex and gender	Not Applicable
Reporting on race, ethnicity, or other socially relevant groupings	Not Applicable
Population characteristics	Not Applicable
Recruitment	Not Applicable
Ethics oversight	Not Applicable

Note that full information on the approval of the study protocol must also be provided in the manuscript.

Field-specific reporting

Please select the one below that is the best fit for your research. If you are not sure, read the appropriate sections before making your selection.

☒ Life sciences ☐ Behavioural & social sciences ☐ Ecological, evolutionary & environmental sciences

For a reference copy of the document with all sections, see nature.com/documents/nr-reporting-summary-flat.pdf

Life sciences study design

All studies must disclose on these points even when the disclosure is negative.

Sample size	Power analysis was used to determine the number of animals required for each analysis based on the previous biochemical and histological differences that we have found when analyzing basal CMA activity and response to stress in liver, heart and brain in vivo using the same reporter mouse model24. With the calculated sample size and a two-sided type 1 error rate of 5% it was predicted >80% power to detect effects >1.5 in the parameters analyzed.
Data exclusions	None of the animals were excluded from the study.
Replication	Each animal was analyzed separately and at least 3 tissue slices imaged from each organ for replication purposes. Experiments were performed in animals collected at independent days to confirm reproducibility of the findings.
Randomization	The experimental design does not allow for randomization as age and sex were variables in the study.
Blinding	The Investigators were not blinded during the dissection of the tissues, but batches of images were acquired using blind observers and information on sex and age group was then lifted for plotting and statistical analysis.

Reporting for specific materials, systems and methods

We require information from authors about some types of materials, experimental systems and methods used in many studies. Here, indicate whether each material, system or method listed is relevant to your study. If you are not sure if a list item applies to your research, read the appropriate section before selecting a response.

Materials & experimental systems

n/a	Involved in the study
☐	☒ Antibodies
☒	☐ Eukaryotic cell lines
☒	☐ Palaeontology and archaeology
☐	☒ Animals and other organisms
☒	☐ Clinical data
☒	☐ Dual use research of concern
☒	☐ Plants

Methods

n/a	Involved in the study
☒	☐ ChIP-seq
☒	☐ Flow cytometry
☒	☐ MRI-based neuroimaging

Antibodies

Antibodies used

All antibodies used are compiled in Supplementary Table S2 with source, catalogue number, clone (when available) and dilutions or working concentrations.
Antibody (Clone) Species Source Catalogue number Dilution
PRIMARY ANTIBODIES
α-smooth muscle Actin (EPR5368) Rabbit Abcam ab124964 1:1000
Aquaporin-2 (polyclonal) Goat Novus Biologicals NBP170378 1:100
Calbindin (D1I4Q) Rabbit Cell Signaling Technology 13176S 1:500
Caveolin (D46G3) Rabbit Cell Signaling Technology 3267 1:1000
CD68 (FA-11) Rat ThermoFisher Scientific MA5-16674 1:500
Cone Arrestin (polyclonal) Rabbit Millipore Sigma AB15282 1:1000
Dendra (OTI1G6) Mouse Origene TA180094 1:500
Dendra (polyclonal) Rabbit Antibodies-online abin361314 1:1000
GFAP (GA5) Mouse Millipore Sigma MAB360 1:1000
Glucagon (K79bB10) Mouse Millipore Sigma G2654 1:500
Insulin (polyclonal) Guinea pig GeneTex GTX39371 1:1000
LAMP1 (1D4B) Rat Hybridoma Bank 1D4B 1:1000
NeuN (A60) Mouse Millipore Sigma MAB377 1:500
Recoverin (polyclonal) Rabbit Millipore Sigma AB5585 1:1000
S100 (B32.1) Mouse Abcam AB7852 1:500
SECONDARY ANTIBODIES
Alexa Fluor 488-anti rabbit Goat IgG ThermoFisher Scientific A-11008 1:500
Alexa Fluor 488-anti mouse Goat IgG ThermoFisher Scientific A-11001 1:500
Alexa Fluor 488-anti rat Goat IgG ThermoFisher Scientific A-11006 1:500
Alexa Fluor 488-anti guinea pig Goat IgG ThermoFisher Scientific A-11073 1:500
Alexa Fluor 488-anti goat Donkey IgG ThermoFisher Scientific A-11055 1:500
Cyanine3-anti rabbit Goat IgG ThermoFisher Scientific A-10520 1:500
Cyanine3-anti mouse Goat IgG ThermoFisher Scientific A-10521 1:500
Cyanine3-anti rat Goat IgG ThermoFisher Scientific A-10522 1:500
Cyanine5-anti rabbit Goat IgG ThermoFisher Scientific A-10523 1:500
Cyanine5-anti mouse Goat IgG ThermoFisher Scientific A-10524 1:500
Cyanine5-anti rat Goat IgG ThermoFisher Scientific A-10525 1:500

Validation

All the antibodies used are commercially available and validated by the manufacturers.
PRIMARY ANTIBODIES
α-smooth muscle Actin (EPR5368) https://www.abcam.com/en-us/products/primary-antibodies/alpha-smooth-muscle-actin-antibody-epr5368-ab124964
Aquaporin-2 (polyclonal) https://www.novusbio.com/search?keywords=NBP170378
Calbindin (D1I4Q) https://www.cellsignal.com/products/primary-antibodies/calbindin-d1i4q-xp-rabbit-mab/13176
Caveolin (D46G3) https://www.cellsignal.com/products/primary-antibodies/caveolin-1-d46g3-xp-rabbit-mab/3267
CD68 (FA-11) https://www.thermofisher.com/antibody/product/CD68-Antibody-clone-FA-11-Monoclonal/MA5-16674
Cone Arrestin (polyclonal) https://www.sigmaaldrich.com/US/en/product/mm/ab15282
Dendra (OTI1G6) https://www.origene.com/catalog/antibodies/tag-antibodies/ta180094-mouse-monoclonal-dendra2-antibody-clone-oti1g6
Dendra (polyclonal) https://www.antibodies-online.com/antibody/361314/anti-Dendra+2+antibody/
GFAP (GA5) https://www.sigmaaldrich.com/US/en/product/mm/mab360
Glucagon (K79bB10) https://www.sigmaaldrich.com/US/en/product/sigma/g2654
Insulin (polyclonal) https://www.genetex.com/Product/Detail/Insulin-antibody/GTX39371?srsltid=AfmBOop2gljwm8lmQygBPIfrbxaRxIVWf6-5VEP89hp4Ek-R02CE_dZR
LAMP1 (1D4B) https://dshb.biology.uiowa.edu/1D4B
NeuN (A60) https://www.sigmaaldrich.com/US/en/product/mm/mab377
Recoverin (polyclonal) https://www.sigmaaldrich.com/US/en/substance/antirecoverinantibody1234598765
S100 (B32.1) https://www.abcam.com/en-us/products/primary-antibodies/s100-antibody-b321-ab7852

SECONDARY ANTIBODIES
Alexa Fluor 488-anti rabbit https://www.thermofisher.com/antibody/product/Goat-anti-Rabbit-IgG-H-L-Cross-Adsorbed-Secondary-Antibody-Polyclonal/A-11008

Alexa Fluor 488-anti mouse https://www.thermofisher.com/antibody/product/Goat-anti-Mouse-IgG-H-L-Cross-Adsorbed-Secondary-Antibody-Polyclonal/A-11001
Alexa Fluor 488-anti rat https://www.thermofisher.com/antibody/product/Goat-anti-Rat-IgG-H-L-Cross-Adsorbed-Secondary-Antibody-Polyclonal/A-11006
Alexa Fluor 488-anti guinea pig https://www.thermofisher.com/antibody/product/Goat-anti-Guinea-Pig-IgG-H-L-Highly-Cross-Adsorbed-Secondary-Antibody-Polyclonal/A-11073
Alexa Fluor 488-anti goat https://www.thermofisher.com/antibody/product/Donkey-anti-Goat-IgG-H-L-Cross-Adsorbed-Secondary-Antibody-Polyclonal/A-11055
Cyanine3-anti rabbit https://www.thermofisher.com/antibody/product/Goat-anti-Rabbit-IgG-H-L-Cross-Adsorbed-Secondary-Antibody-Polyclonal/A10520
Cyanine3-anti mouse https://www.thermofisher.com/antibody/product/Goat-anti-Mouse-IgG-H-L-Cross-Adsorbed-Secondary-Antibody-Polyclonal/A10521
Cyanine3-anti rat https://www.thermofisher.com/antibody/product/Goat-anti-Rat-IgG-H-L-Cross-Adsorbed-Secondary-Antibody-Polyclonal/A10522
Cyanine5-anti rabbit https://www.thermofisher.com/antibody/product/Goat-anti-Rabbit-IgG-H-L-Cross-Adsorbed-Secondary-Antibody-Polyclonal/A10523
Cyanine5-anti mouse https://www.thermofisher.com/antibody/product/Goat-anti-Mouse-IgG-H-L-Cross-Adsorbed-Secondary-Antibody-Polyclonal/A10524
Cyanine5-anti rat https://www.thermofisher.com/antibody/product/Goat-anti-Rat-IgG-H-L-Cross-Adsorbed-Secondary-Antibody-Polyclonal/A10525

Animals and other research organisms

Policy information about studies involving animals; ARRIVE guidelines recommended for reporting animal research, and Sex and Gender in Research

Laboratory animals	KFERQ-Dendra2 transgenic male and female C57BL/6J mice24 at 4-6 months and 24-28 months of age were used in this work. all mice were genotyped post euthanization and genotype of progenitors was performed at weaning and re-confirmed postbreeding to correct for any possible misplacement during husbandry. Mice were housed in ventilated cages with no more than 5 mice per cage on a 12h light/dark cycle at 23°C, 40-60% humidity with ad libitum access to water and standard rodent chow in our pathogen-free barrier facility along with sentinel cages. KFERQ-Dendra was generated KFERQ-Dendra mice were generated by donor egg injection in wild-type FVB mice using the pRP.ExSi plasmid backbone with the insert coding for 11 amino acids including the KFERQ sequence of RNase A in frame with the sequence of Dendra 2 under the hybrid promoter CAGG as described in the text.
Wild animals	No wild animals were used in the study
Reporting on sex	Male and female mice were used in this study and results were reported separately and statistically compared to account for sex as a biological variable. Whenever possible same number of males and females were included in the analysis. Mice sex was determined using the anogenital distance whereby the distance between the anus and the external genitalia is greater in males than females. Sex was confirmed upon euthanasia and organ dissection by identification of ovary and testes in females and males, respectively.
Field-collected samples	No field collected samples were used in the study
Ethics oversight	All mouse procedures were approved by the Institutional Animal Care and Use Committee of Albert Einstein College of Medicine.

Note that full information on the approval of the study protocol must also be provided in the manuscript.

Plants

Seed stocks	*Report on the source of all seed stocks or other plant material used. If applicable, state the seed stock centre and catalogue number. If plant specimens were collected from the field, describe the collection location, date and sampling procedures.*
Novel plant genotypes	*Describe the methods by which all novel plant genotypes were produced. This includes those generated by transgenic approaches, gene editing, chemical/radiation-based mutagenesis and hybridization. For transgenic lines, describe the transformation method, the number of independent lines analyzed and the generation upon which experiments were performed. For gene-edited lines, describe the editor used, the endogenous sequence targeted for editing, the targeting guide RNA sequence (if applicable) and how the editor was applied.*
Authentication	*Describe any authentication procedures for each seed stock used or novel genotype generated. Describe any experiments used to assess the effect of a mutation and, where applicable, how potential secondary effects (e.g. second site T-DNA insertions, mosiacism, off-target gene editing) were examined.*